

# Journal of Geophysical Research: Solid Earth

JGR

## RESEARCH ARTICLE

10.1029/2017JB015325

**Key Points:**

- We estimate full moment tensors for 116 events: nuclear explosions, volcanic events, and earthquakes
- We apply a new method for calculating and visualizing uncertainties in moment tensors and their source types
- Based on detailed analysis of 29 Nevada Test Site events, we document important choices in moment tensor inversions

**Supporting Information:**

- Supporting Information S1

**Correspondence to:**

C. Alvizuri,  
celso.alvizuri@gmail.com

**Citation:**

Alvizuri, C., Silwal, V., Krischer, L., & Tape, C. (2018). Estimation of full moment tensors, including uncertainties, for nuclear explosions, volcanic events, and earthquakes. *Journal of Geophysical Research: Solid Earth*, 123. <https://doi.org/10.1029/2017JB015325>

Received 6 DEC 2017

Accepted 7 APR 2018

Accepted article online 19 APR 2018

## Estimation of Full Moment Tensors, Including Uncertainties, for Nuclear Explosions, Volcanic Events, and Earthquakes

**Celso Alvizuri<sup>1,2</sup> , Vipul Silwal<sup>1</sup> , Lion Krischer<sup>3</sup> , and Carl Tape<sup>1</sup> **

<sup>1</sup>Geophysical Institute and Department of Geosciences, University of Alaska Fairbanks, Fairbanks, AK, USA, <sup>2</sup>Institute of Earth Sciences, University of Lausanne, Lausanne, Switzerland, <sup>3</sup>Institut für Geophysik, ETH Zürich, Zürich, Switzerland

**Abstract** A seismic moment tensor is a  $3 \times 3$  symmetric matrix that provides a compact representation of a seismic source. We develop an algorithm to estimate moment tensors and their uncertainties from observed seismic data. For a given event, the algorithm performs a grid search over the six-dimensional space of moment tensors by generating synthetic waveforms for each moment tensor and then evaluating a misfit function between the observed and synthetic waveforms. “The” moment tensor  $M_0$  for the event is then the moment tensor with minimum misfit. To describe the uncertainty associated with  $M_0$ , we first convert the misfit function to a probability function. The uncertainty, or rather the confidence, is then given by the “confidence curve”  $\mathcal{P}(V)$ , where  $\mathcal{P}(V)$  is the probability that the true moment tensor for the event lies within a certain neighborhood of  $M$  that has fractional volume  $V$ . The area under the confidence curve provides a single, abbreviated “confidence parameter” for  $M_0$ . We apply the method to data from events in different regions and tectonic settings: 17 nuclear explosions and 12 earthquakes at the Nevada Test Site, 63 small ( $M_w < 2.5$ ) events at Uturuncu volcano in Bolivia, and 21 moderate ( $M_w > 4$ ) earthquakes in the southern Alaska subduction zone. Characterization of moment tensor uncertainties puts us in better position to discriminate among moment tensor source types and to assign physical processes to the events.

### 1. Introduction

The seismic moment tensor is a  $3 \times 3$  symmetric matrix that characterizes a seismic source within the Earth. Its six parameters can be separated into three eigenvalues that characterize the magnitude and moment tensor “source type” and three angles (e.g., strike, dip, and rake) that provide the moment tensor orientation. For most earthquakes, the source type is a four-parameter double-couple moment tensor that represents shear faulting. For exotic events, the source is characterized by a six-parameter “full” moment tensor, whose eigenvalues may represent, for example, an explosion, an implosion, or an oblique opening (or closing) crack (Aki & Richards, 2002).

Full moment tensors have been used to characterize events in a range of settings, including earthquakes, volcanoes, glaciers, landslides, hydraulic fracturing, mine collapses, and nuclear explosions (Alvizuri & Tape, 2016, Table 1). In most studies, the goal has been to estimate the moment tensor  $M_0$  that provides synthetic seismograms that best fit a set of observed seismograms. The fit is quantified by a misfit function defined on the space of moment tensors; its minimum occurs at  $M_0$ .

In the past decade, efforts have been made to characterize uncertainties of moment tensors. Some studies have estimated the uncertainties by repeatedly solving for  $M_0$  using different subsets of data (bootstrapping or related Monte Carlo approaches; Ford et al., 2009; Pesicek et al., 2012, 2016; Ross et al., 2015; Šílený & Milev, 2006; Vavryčuk, 2011). Other studies have provided a view of how the misfit function varied over the full space of moment tensor source types (Alvizuri & Tape, 2016; Boyd et al., 2015; Ford et al., 2010; Nayak & Dreger, 2014). To our knowledge, Stähler and Sigloch (2014) is the only study to have formally accounted for uncertainties, by generating moment tensor samples of a posterior probability density.

The goal of this study is to estimate moment tensor uncertainties for three sets of previously studied events (Table 1). Following Tape and Tape (2016), we represent moment tensor uncertainties in the form of a confidence curve that expresses the concentration of probability in moment tensor space near  $M_0$ . We build upon three recent studies: Tape and Tape (2016), which established the theory for confidence curves; Silwal and Tape (2016), which estimated confidence curves for double-couple moment tensors; and Alvizuri and Tape

**Table 1**

Summary of Data Used in 116 Moment Tensor Inversions in This Study

Set of events	Number of events	Reference	First-motion polarities	P waveforms	Surface waves	Depth search
Nevada Test Site, nuclear explosions	17	Ford et al. (2009)	—	(Y)	Y	—
Nevada Test Site, earthquakes	12	Ford et al. (2009)	—	Y	Y	Y
Cavity collapse events	3	Ford et al. (2009)	—	—	Y	—
Uturuncu volcano	63	Alvizuri and Tape (2016)	Y	Y	(Y)	—
Alaska earthquakes	21	Silwal and Tape (2016)	—	Y	Y	Y <sup>a</sup>

Note. The symbol "(Y)" indicates that the data were used for only a subset of events.

<sup>a</sup>A depth search was performed in Silwal and Tape (2016) using the double-couple constraint; we fix those depths for our full moment tensor inversions.

(2016), which estimated a catalog of full moment tensors for volcanic events. In our examination of earthquakes and nuclear explosions from the Nevada Test Site (NTS), we use the same 29 events as in Ford et al. (2009). Relative to Ford et al. (2009), however, we use more stations, and we use body waves (in addition to surface waves). We also use a broader band pass for surface waves (minimum period 7 s) and provide an alternative characterization of moment tensor uncertainties.

## 2. Data

We examine events from three previous studies (Table 1): 29 earthquakes and nuclear tests at the Nevada Test Site (Ford et al., 2009, Table 1) 63 events at Uturuncu volcano in Bolivia (Alvizuri & Tape, 2016, Table 4), and 21 earthquakes in southern Alaska (Silwal & Tape, 2016, Table 4). Figure 1 shows the three regions and the stations used in the moment tensor inversions. For completeness, we also examine the three collapse events studied by Ford et al. (2009). The catalog of Bennett et al. (2010), shown in Figure S1 in the supporting information for events since 1988, contains additional events besides those considered in the studies of Ford et al. (2009) and ours.

For the Alaska and Uturuncu data sets, all waveforms are openly available from the Incorporated Research Institutions for Seismology (IRIS) Data Management Center. For the NTS events, some of the waveforms are openly available from IRIS and the Northern California Data Center, while other waveforms are from the database of Walter et al. (2006). A summary of available waveforms for the NTS events is provided in Table 2, where we see increasing numbers of broadband seismic stations in the 1990s.

All waveforms were downloaded and processed using ObsPy, a Python-based package for seismology (Beyreuther et al., 2010; Krischer et al., 2015). The processing steps for each event were as follows: (1) Obtain three-component waveforms and metadata from the IRIS Data Management Center, the Northern California Earthquake Data Center, or Walter et al. (2006); the time interval is 100 s before the origin time to 600 s after the origin time. (2) Remove instrument response. (3) Rotate horizontal components to radial and transverse directions. Additional processing steps, such as cutting time windows and additional band-pass filtering, were applied during the moment tensor inversions.

We use high-frequency *P* waves for the Uturuncu and NTS events. Within the misfit function, described next, we make waveform measurements between observed and synthetic *P* waves. These measurements are more reliable when we align the *P* waves on the observed *P* arrival time. For the Uturuncu events we use arrival times from Keyson and West (2013). For the NTS events we pick arrival times for the IRIS stations and use the arrival times in Walter et al. (2006) for the Lawrence Livermore National Laboratory stations. For the Uturuncu events we use first-motion polarity measurements from Alvezuri and Tape (2016). From our experiences, it is important to use first-motion polarities (and observed arrival times, for alignment with synthetics) when analyzing small ( $M_w \leq 3$ ) events with high-frequency ( $f \geq 1$  Hz) waveforms. Previous work demonstrating the combination of waveforms and first-motion polarities include Ford et al. (2012) and Chiang et al. (2014).

## 3. Methods

Our seismic moment tensor inversion requires specifying a misfit function between observed seismograms and synthetic (or "modeled") seismograms. Synthetic seismograms are calculated using a model of the source—in our case, a moment tensor—and a model of Earth's structure—in our case, a layered model.

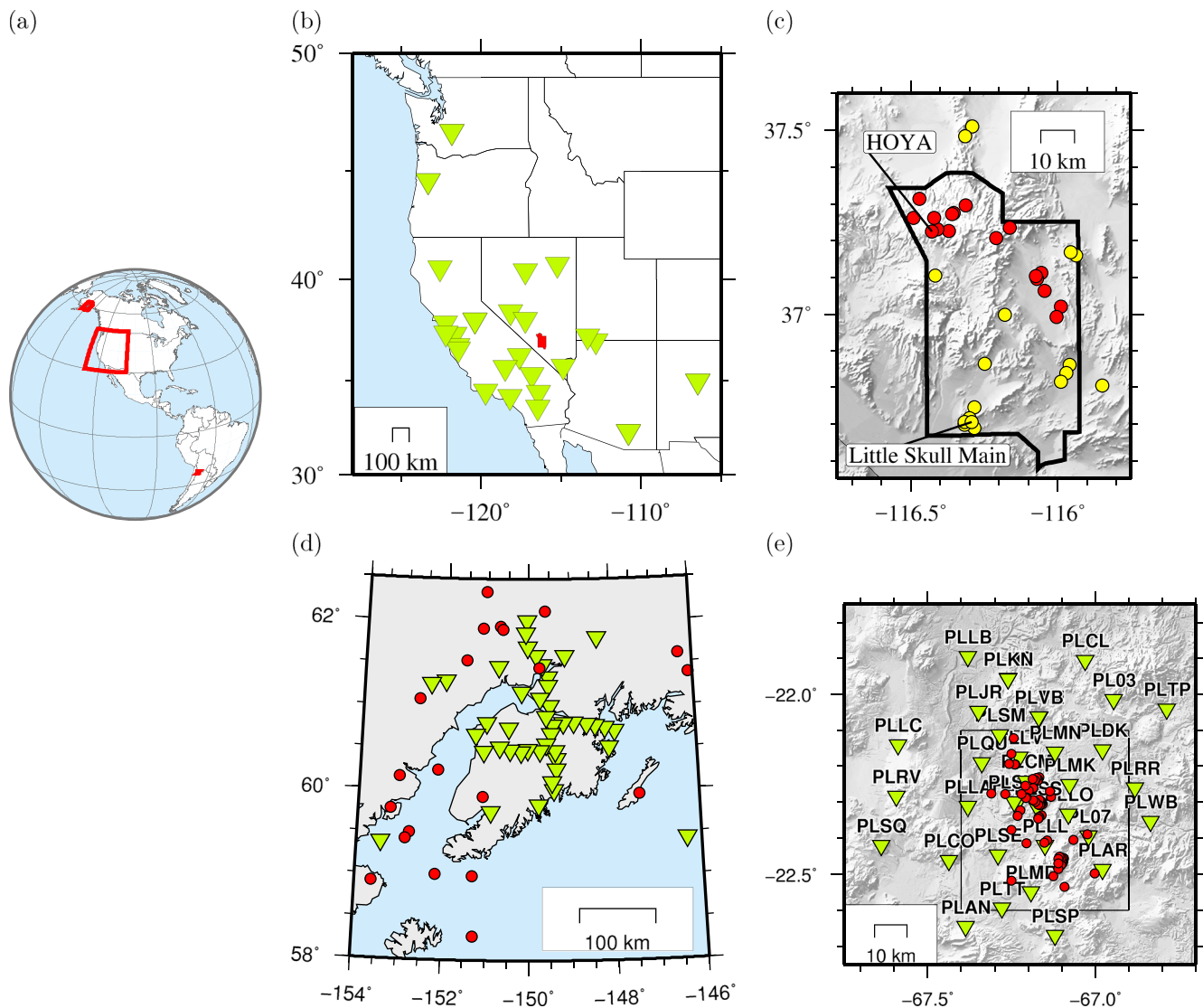


**Figure 1.** Three study regions of the Nevada Test Site, Alaska, and Bolivia. (a) Global perspective showing our three study regions. (b) Western United States, with the Nevada Test Site outlined. Triangles denote the stations used within our moment tensor inversions for the 17 nuclear explosions. (c) Nevada Test Site. Nuclear explosions (17) are red, and earthquakes (12) are yellow. (d) Twenty-one earthquakes in southern Alaska (Silwal & Tape, 2016). (e) Sixty-three events at Uturuncu volcano, Bolivia (Alvizuri & Tape, 2016).

For the NTS events, we use the same three-layered model as used in Ford et al. (2009, Table 2), which is the model of Song et al. (1996, Table 1) but with explicit attenuation. The crust is represented by a shallow 2.5-km thick layer overlying a 32.5-km thick layer, which in turn overlies a mantle halfspace. For the Uturuncu events we use the same homogeneous model as in Alvizuri and Tape (2016); for the Alaska earthquakes we use the same layered model as in Silwal and Tape (2016). We calculate synthetic seismograms for a range of source depths and source-station distances using the frequency-wavenumber method of Haskell (1964) and Zhu and Rivera (2002). The source origin times and hypocenters are assumed to be fixed.

The misfit function we use, from Zhu and Helmberger (1996), measures integrated differences between observed and synthetic velocity seismograms within five time windows: *P* wave on vertical and radial components, Rayleigh wave on vertical and radial components, and Love wave on transverse component. Prior to calculating the waveform difference, we allow the synthetic seismograms to be shifted in time to maximize the cross correlation with observed seismograms. For each station, three time shifts are allowed, for the *P*, Rayleigh, and Love waves. The differing time shifts are allowed because these waves are sensitive to different

**Table 2**

Nuclear Explosions (17), Earthquakes (12), and Collapse Events (3) From Ford et al. (2009), Reexamined in This Study

Event name	Origin time	Longitude	Latitude	Catalog		Inversion depth (km)	No. of stations used (# available)			
				depth (km)	S02		IRIS	NCECD	LLNL	Total
KERNVILLE	1988-02-15 18:10:00.09	-116.4720	37.3140	0.542	S02	1	3 (5)	3 (4)	7 (10)	13 (19)
AMARILLO	1989-06-27 15:30:00.02	-116.3540	37.2750	0.640	S02	1	4 (7)	3 (8)	5 (8)	12 (23)
DISKO ELM	1989-09-14 15:00:00.10	-116.1640	37.2360	0.261	S02	1	2 (8)	1 (7)	6 (14)	9 (29)
HORNITOS	1989-10-31 15:30:00.09	-116.4920	37.2630	0.564	S02	1	5 (11)	3 (8)	7 (16)	15 (35)
BARNWELL	1989-12-08 15:00:00.09	-116.4100	37.2310	0.601	S02	1	4 (11)	4 (11)	4 (16)	12 (38)
METROPOLIS	1990-03-10 16:00:00.08	-116.0560	37.1120	0.469	S02	1	4 (10)	4 (10)	4 (15)	12 (35)
BULLION	1990-06-13 16:00:00.09	-116.4210	37.2620	0.674	S02	1	3 (11)	4 (10)	2 (16)	9 (37)
AUSTIN	1990-06-21 18:15:00.00	-116.0050	36.9930	0.350	S02	1	5 (11)	1 (8)	5 (16)	11 (35)
HOUSTON	1990-11-14 19:17:00.07	-116.3720	37.2270	0.594	S02	1	3 (13)	4 (8)	6 (14)	13 (35)
COSO	1991-03-08 21:02:45.08	-116.0750	37.1040	0.417	S02	1	5 (21)	1 (2)	8 (17)	14 (40)
BEXAR	1991-04-04 19:00:00.00	-116.3140	37.2960	0.629	S02	1	9 (25)	0 (0)	8 (17)	17 (42)
HOYA	1991-09-14 19:00:00.08	-116.4290	37.2260	0.658	S02	1	9 (25)	2 (10)	7 (17)	18 (52)
LUBBOCK	1991-10-18 19:12:00.00	-116.0460	37.0630	0.457	S02	1	8 (23)	1 (8)	5 (16)	14 (47)
BRISTOL	1991-11-26 18:35:00.07	-116.0700	37.0960	0.457	S02	1	7 (23)	2 (7)	8 (17)	17 (47)
JUNCTION	1992-03-26 16:30:00.00	-116.3610	37.2720	0.622	S02	1	9 (27)	2 (9)	4 (17)	15 (53)
HUNTERS TROPHY	1992-09-18 17:00:00.08	-116.2110	37.2070	0.385	S02	1	5 (34)	4 (27)	3 (19)	12 (80)
DIVIDER	1992-09-23 15:04:00.00	-115.9890	37.0210	0.340	S02	1	5 (36)	6 (31)	1 (14)	12 (81)
Little Skull Main	1992-06-29 10:14:21.89	-116.2722	36.6385	9.070	CI	10	8 (50)	6 (30)	1 (11)	15 (91)
Little Skull Aftershock	1992-07-05 06:54:10.72	-116.0178	36.6767	5.070	CI	5	7 (50)	5 (27)	2 (14)	14 (91)
Timber Mountain	1995-07-31 12:34:45.03	-116.2057	37.1363	4.487	CI	4	26 (88)	12 (69)	0 (9)	38 (166)
Amargosa	1996-09-05 08:16:56.09	-116.3378	36.6827	9.070	CI	9	17 (80)	13 (108)	0 (0)	30 (188)
Groom Pass	1997-04-26 01:49:35.58	-115.9220	37.1987	5.000	US	5	28 (75)	13 (100)	0 (43)	41 (218)
Indian Springs	1997-06-14 19:48:19.93	-115.8133	36.5172	5.793	CI	6	18 (99)	7 (108)	0 (0)	25 (207)
Calico Fan	1997-09-12 13:36:54.20	-116.1182	36.8422	6.037	CI	6	34 (129)	15 (125)	1 (27)	50 (281)
Warm Springs	1998-12-12 01:41:30.33	-116.1605	37.5437	0.0	REN	1	29 (146)	10 (156)	0 (21)	39 (323)
Frenchman Flat 1	1999-01-23 03:00:34.82	-116.0277	36.7640	0.0	REN	1	11 (145)	0 (135)	0 (57)	11 (337)
Frenchman Flat 2	1999-01-27 10:44:17.80	-115.4578	36.7790	5.000	US	5	35 (143)	19 (162)	1 (56)	55 (361)
Little Skull	2002-06-14 12:40:45.82	-116.3448	36.6438	9.653	CI	10	62 (197)	20 (334)	0 (70)	82 (601)
Ralston	2007-01-24 11:30:16.10	-117.0986	37.4133	6.100	NN	6	65 (674)	23 (580)	0 (0)	88 (1254)
ATRISCO Hole	1982-08-05 14:21:00	-116.0065	37.0842	0.640	S02	1	3 (3)	0 (0)	0 (3)	3 (6)
Trona Mine 1	1995-02-03 15:26:10.69	-109.6400	41.5300	1.000	US	1	8 (51)	0 (43)	1 (15)	9 (109)
Trona Mine 2	2000-01-30 14:46:51.31	-109.6800	41.4600	1.000	US	1	23 (137)	3 (151)	9 (31)	35 (319)

Note. Origin times and epicenters are from Ford et al. (2009). Depths are from either Springer et al. (2002) (S02) or from the US Geological Survey Earthquake Catalog, who label the contributing source as follows: US (National Earthquake Information Center), CI (Southern California Seismic Network), REN (University of Nevada Reno), or NN (Nevada Seismological Laboratory). LLNL = Lawrence Livermore National Laboratory. Dates are formatted as year-month-day.

parts of Earth structure. By allowing for different time shifts, we are recognizing that our layered Earth structural models cannot adequately predict the traveltimes for seismic waves. Additional discussion of time shifts can be found in Silwal and Tape (2016).

For our moment tensor inversions, we use the “cut-and-paste” code of Zhao and Helmberger (1994), Zhu and Helmberger (1996), and Zhu and Ben-Zion (2013), with some modifications. Our misfit function is given by

$$\Phi(M) = m \frac{\Phi_p(M)}{N_p} + (1 - m) \frac{\Phi_w(M)}{\| \mathbf{u} \|_{L1}} \quad (1)$$

where  $\Phi_p(M)$  is the L1 misfit of polarities,  $\Phi_w(M)$  is the L1 misfit of waveform differences (e.g., Silwal & Tape, 2016),  $N_p$  is the number of polarities used, and  $m$  is a weight factor to balance the contributions of polarity differences and waveform differences. We also use an efficient grid search over moment tensor space, described below.

### 3.1. Parameterization of Moment Tensors

For any triple  $\hat{\Lambda} = (\lambda_1, \lambda_2, \lambda_3)$ , we let  $[\hat{\Lambda}]$  be the diagonal matrix whose diagonal entries are  $\lambda_1, \lambda_2, \lambda_3$ . A moment tensor  $M$  is a  $3 \times 3$  symmetric matrix and hence can be expressed as  $M = [\hat{\Lambda}]_U = U[\hat{\Lambda}]U^{-1}$  for some  $[\hat{\Lambda}]$  and for some rotation matrix  $U$ . The numbers  $\lambda_1, \lambda_2, \lambda_3$  are in fact the eigenvalues of  $M$ , and they are assumed to be in descending order. The source type of  $M$  is the normalized eigenvalue triple  $\Lambda = \hat{\Lambda}/\|\hat{\Lambda}\|$ . The source types for all moment tensors make up the (fundamental) lune of the unit sphere. The lune has the positive isotropic source type  $(1, 1, 1)/\sqrt{3}$  at its north pole, the negative isotropic source type  $(-1, -1, -1)/\sqrt{3}$  at its south pole, and the double couple  $(1, 0, -1)/\sqrt{2}$  at its center. Source types—or beach ball patterns—fall into four regions on the lune (Tape & Tape, 2013, Figure S1): (1) all-red beach balls ( $\lambda_3 > 0$ ), (2) red beach balls with white caps ( $\lambda_2 > 0 > \lambda_3$ ), (3) white beach balls with red caps ( $\lambda_1 > 0 > \lambda_2$ ), and (4) all-white beach balls ( $\lambda_1 < 0$ ). (The traditional binary coloring of beach balls does not completely capture the variations in amplitude of the source radiation pattern.)

A moment tensor is determined by six parameters. In searching moment tensor space, however, we separate magnitude from the five other parameters and so we need only parameterize the 5-D space of moment tensors having unit magnitude. Three parameters specify the orientation  $U$  of the moment tensor, and two specify the source type  $\Lambda$ . One's first inclination might be to use the strike, rake, and dip angles to parameterize  $U$  and to use lune longitude  $\gamma$  and latitude  $\delta$  to parameterize  $\Lambda$ , but those choices are not the most efficient. We therefore replace the dip angle  $\theta$  with  $h = \cos \theta$ , and we replace  $\gamma$  and  $\delta$  with the closely related parameters  $v$  and  $w = 3\pi/8 - u$ , where  $u$  and  $v$  are as in section 5 of Tape and Tape (2015). We then have  $U = U(\kappa, \sigma, h)$  and  $\Lambda = \Lambda(v, w)$ . Thus, we are parameterizing moment tensors of unit norm using the following coordinates:

1.  $v$ , related to lune longitude,  $-1/3 \leq v \leq 1/3$
2.  $w$ , related to lune latitude,  $-3\pi/8 \leq w \leq 3\pi/8$
3. strike angle  $\kappa$ ,  $0^\circ \leq \kappa < 360^\circ$
4. rake (or slip) angle  $\sigma$ ,  $-90^\circ \leq \sigma \leq 90^\circ$
5.  $h = \cos \theta$ ,  $0 < h \leq 1$ , corresponding to dip  $\theta$  ranging from  $0^\circ$  to  $90^\circ$

The parameterization is  $(v, w, \kappa, \sigma, h) \rightarrow [\hat{\Lambda}(v, w)]_{U(\kappa, \sigma, h)}$ . It is uniform, in the sense that a uniform distribution of 5-tuples  $(v, w, \kappa, \sigma, h)$  in the coordinate domain corresponds to a uniform distribution in the moment tensor space. Stated otherwise, volumes (i.e., 5-volumes) in the coordinate domain are proportional to the corresponding volumes of moment tensors (Tape & Tape, 2015, equation (29)). Among other things, the uniformity of the parameterization is used in defining the moment tensor probability from the misfit function.

### 3.2. Grid Search for the Optimal Moment Tensor

We perform two grid searches to obtain the best-fitting moment tensor  $M_0$ . The first is a coarse grid search of 100,000 moment tensors, with each moment tensor searching over a range of  $M_w$  magnitudes in 0.1 intervals and source depths in 1-km intervals. For the 17 nuclear explosions, we used an  $M_w$  interval of 0.01. This first search provides the best-fitting magnitude and depth.

The second search is a fine grid search of 10,000,000 moment tensors, with each moment tensor represented by  $M = (v, w, \kappa, \sigma, h)$ . The tensors are uniformly distributed in the sense that equal volumes contain approximately equal numbers of tensors, but the tensors are not necessarily at grid points of a regular grid. For each moment tensor in the grid search, we evaluate the misfit function. If first-motion polarity measurements are used, we also compute the misfit between observed and predicted first-motion polarities for each moment tensor in the grid.

We also perform a third grid search for visualization purposes: to make the type of lune plot shown in Figure 5. This involves evaluating a regular grid of over 20,000,000 moment tensors.

### 3.3. Confidence Curves for Moment Tensors

Our grid search of moment tensor space provides a global minimum  $M_0$  of the misfit function and reveals how the misfit function varies over the full space. Tape and Tape (2016) showed how to distill the complexity of a misfit function into a “confidence curve”  $\mathcal{P}(V)$  that gives the probability as a function of fractional volume

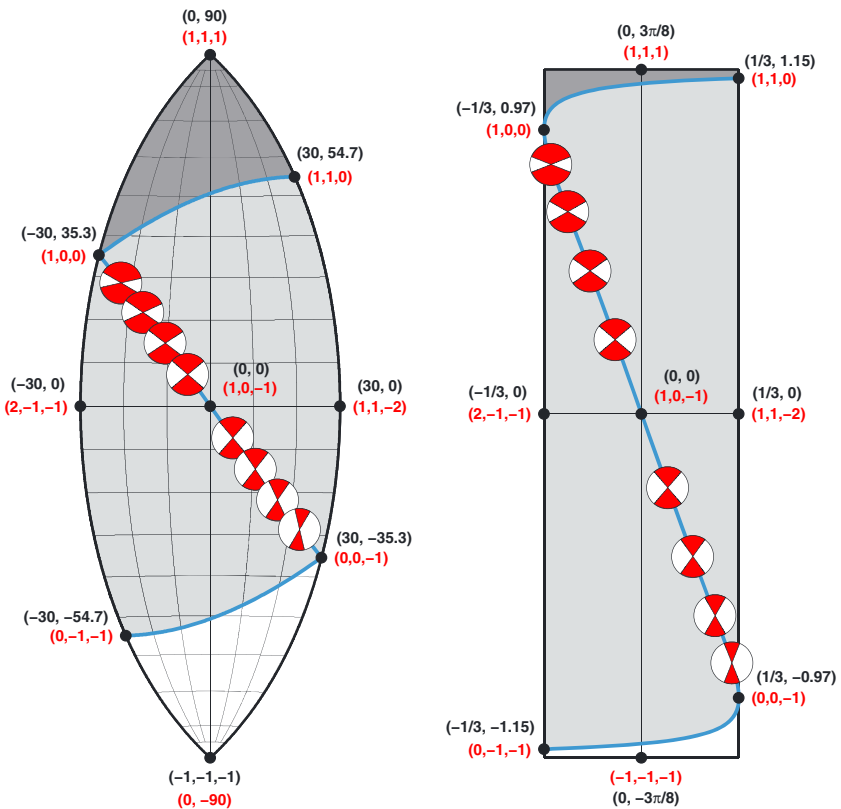


**Figure 2.** Comparison of moment tensor source-type plots for the lune (left) and the vw rectangle (right) (Tape & Tape, 2012, 2015). Source-type plots represent the normalized eigenvalues of moment tensors. The blue arcs on the lune are the arcs  $\lambda_1 = 0$ ,  $\lambda_2 = 0$ , and  $\lambda_3 = 0$ . Selected eigenvalue triples (black dots) are indicated, with the understanding that the triples (red labels) need to be normalized. The positive isotropic source  $(1, 1, 1)$  is at the top, the negative isotropic source  $(-1, -1, -1)$  is at the bottom, and the double couple  $(1, 0, -1)$  is at the center of the lune. On the lune each source type is labeled (black) with its lune longitude  $\gamma$  and lune latitude  $\delta$ . On the vw rectangle each source is labeled with its vw coordinates. Eight beach balls with  $\lambda_2 = 0$  are shown.

of moment tensor space, measured from  $M_0$ . The slope of the confidence curve at the origin ( $M_0$ ) is proportional to the probability density  $p(M_0)$ . The area under the confidence curve is the confidence parameter  $\mathcal{P}_{av}$ . The confidence curve  $\mathcal{P}(V)$  is constructed from two functions  $\hat{V}(\omega)$  and  $\hat{P}(\omega)$  (Silwal & Tape, 2016, Figure 4). The number  $\hat{V}(\omega)$  is the fractional volume of the set of moment tensors within angular distance  $\omega$  of  $M_0$ , and  $\hat{P}(\omega)$  is the probability associated with that same set.

The function  $\hat{V}(\omega)$  depends on the moment tensor context. In Silwal and Tape (2016) the context was double couple moment tensors, and the derivative  $\hat{V}'(\omega)$  took on a distinctive mesa-like shape. In the current context of full moment tensors, the derivative is  $\hat{V}'(\omega) = \frac{8}{3\pi} \sin^4 \omega$  (Tape & Tape, 2016, equation (29)).

As described in Silwal and Tape (2016), a choice of a constant  $k$  is needed when converting the misfit function  $\Phi$  into a probability density  $p \propto e^{-k\Phi}$ . This choice of  $k$  ultimately impacts the function  $\hat{P}(\omega)$ .

### 3.4. Probability Density for Moment Tensor Source Type

Either the lune or the vw-coordinate rectangle (vw from section 3.1) can be used to depict all moment tensor source types. Figure 2 compares the two depictions. As is clear in the figure, regions of the lune near the lune boundary are compressed when depicted in the vw rectangle. These are the regions where at least two of the eigenvalues  $\lambda_1, \lambda_2, \lambda_3$  nearly coincide. The compression is extreme for the regions of the lune near either isotropic point.

The lune is more transparent, or at least more familiar, than the vw rectangle, and it has the nice feature that distances on the lune are closely related to distances between moment tensors. Precisely, the great circle arc length between points  $\Lambda_1$  and  $\Lambda_2$  on the lune is the same as the angle, in matrix space, between the moment tensors  $[\Lambda_1]_U$  and  $[\Lambda_2]_U$  (same  $U$  for both). On the other hand, areas on the vw rectangle are proportional

to volumes of moment tensors, as explained below. As a result, a uniform distribution of moment tensors has its source types uniformly distributed in the  $vw$  rectangle. (The converse is false, however; since the  $vw$  rectangle contains no information about moment tensor orientations, a non-uniform distribution of moment tensors might have a uniform distribution of its source types.)

The probability  $P(C)$  of a subset  $C$  of the  $vw$  rectangle is understood to mean the probability that the moment tensor for the seismic event has (the  $vw$  coordinate pair for) its source type in  $C$ . Thus,

$$P(C) \approx \frac{\sum_{\Lambda_i \in C} p(M_i)}{\sum_{i=1}^n p(M_i)} \quad (2)$$

where  $M_i$  is the  $i$ th tensor of the  $n = 10^7$  tensors used in the fine grid search (section 3.2), where  $\Lambda_i$  is the source type of  $M_i$  and where  $p(M)$  is the probability density at  $M$  in moment tensor space, as given at the end of section 3.3. The probability density at a point  $(v, w)$  in the  $vw$  rectangle is then  $p(v, w) \approx P(C)/\text{area}(C)$ , where  $C$  is a small square centered at  $(v, w)$  and contained in the  $vw$  rectangle.

The  $vw$  rectangle has the critical property that areas in it are proportional to volumes in moment tensor space (equation (29) of Tape & Tape, 2015). Precisely, for any subset  $A$  of the  $vw$  rectangle, the 5-volume of the set of unit moment tensors having source type in  $A$  is  $2\pi^2 \text{area}(A)$ . Probability density in the  $vw$  rectangle is therefore the “right” concept, in the sense that it is essentially a ratio of probability to 5-volume, and it is therefore comparing the probability inferred from the seismograms to the probability for random moment tensors. Hence, we show the probability density on the  $vw$  plane (Figure 5c); the probability density on the lune would be misleading.

We regard the point  $(v_x, w_x)$  that has the maximum probability density  $p(v, w)$  as being the most probable source type. Note that  $(v_x, w_x)$  will in general differ from the point  $(v_0, w_0)$  that gives the source type for the overall best-fitting moment tensor  $M_0$ . The point  $(v_x, w_x)$  is a better expression of the most likely source type, in the sense that, by allowing orientations to vary, it incorporates the probabilities of all moment tensors having the source type in question.

#### 4. Choices Made for Moment Tensor Inversions

Ideally, we want to find a moment tensor that produces synthetic seismograms that fit all three components of all available broadband seismograms. This is not possible, mainly due to the high-frequency portions of the seismic wavefield that cannot be fit using 1-D (or even 3-D) seismic velocity models. Therefore, the observed and synthetic seismograms are filtered with a minimum period, for example, 10 or 20 s in Ford et al. (2009). Filtering with a maximum period (e.g., 50 s) is also needed in order to suppress contaminating noise at the longest periods. For example, most of the events in Ford et al. (2009) were band-pass filtered 20–50. At these periods, the NTS seismograms exhibit predominantly surface waves, though for larger earthquakes (e.g., Figure S3) there can be significant body wave signals in this band pass. Removal of spurious waveforms or stations further reduces the amount of seismic wavefield that is being fit.

To fit the most of the seismic wavefield, we try to use the broadest period range, the largest number of stations, and a combination of body waves and surface waves. These choices involve substantial exploration of parameters, and they depend strongly on the event magnitude and particular regional settings.

Table 1 summarizes the 116 events considered in this study. The table reveals three different types of data used in the inversions: first-motion  $P$  polarities,  $P$  waveforms, and surface waves (Rayleigh and Love). Ideally, we would use both  $P$  waves and surface waves for all sources, since, taken together, they enhance the aperture of the source radiation recorded by the seismometers. However, in several cases this is not possible due to low signal-to-noise ratio for the waveforms of interest, so some choices need to be made.

We illustrate several choices using the Little Skull Mountain earthquake of 29 June 1992. This earthquake occurred inside the Nevada Test Site (Figure 1c) and is the largest event analyzed by Ford et al. (2009). It is notable for its size ( $M_w > 5$ ) and its occurrence near Yucca Mountain, which, at the time, was under consideration as a storage site for nuclear waste. Reported magnitude values include  $M_s$  5.4 (Gomberg & Bodin, 1994),  $M_L$  5.6 (Harmsen, 1994),  $M_w$  5.6 (Ford et al., 2009; Lohman et al., 2002), and  $M_w$  5.7 (Dziewonski et al., 1981;

Ekström et al., 2012). The Little Skull Mountain earthquake occurred 22 hr after the  $M_w$  7.3 Landers, California, earthquake. Gomberg and Bodin (1994) concluded that seismic waves from the Landers earthquake dynamically triggered the Little Skull Mountain earthquake. Table 1 of Lohman et al. (2002) summarizes several studies of the source parameters of the Little Skull Mountain earthquake.

Moment tensor inversion results for the Little Skull Mountain earthquake were shown in Lohman et al. (2002) and Ford et al. (2009). Lohman et al. (2002) used four stations, with body waves filtered 5–100 s and surface waves filtered 20–100 s. Ford et al. (2009) used seven stations, with surface waves filtered 20–50 s. We perform full moment tensor inversions, including depth searches, using these two different subsets of filtered waveforms. The results (Figures S2 and S3) show a normal fault with very little non-double-couple component. We also perform a depth search for each case and obtain estimates of 12 km (Figure S2b) and 11 km (Figure S3), both of which are close to the traveltimes-derived catalog depth of 9 km (Table 2). For our preferred solution, we use 10 km for the estimated depth, based on consensus from previous studies (Lohman et al., 2002, Table 1).

Our moment tensor inversion for the Little Skull Mountain earthquake uses 15 stations (Table 2) and includes  $P$  waves (periods 5–50 s) and surface waves (periods 10–50 s). The solution is close to double couple, with the best-fitting moment tensor having lune coordinates of  $(\gamma, \delta) = (-5^\circ, 10^\circ)$ . The waveform fits (Figure S4) reflect our preference for including shorter periods, which results in worse waveform fits (i.e., lower VR) because the layered model is a worse approximation at shorter periods. We performed grid searches over different band passes in order to identify the widest possible period range that would provide a stable moment tensor solution. Examples of the influence on the waveform fits of lowering the minimum period are shown in Figures S6–S8, where the minimum period decreases from 10 to 5 s.

Hypocentral depth is an important source parameter, since it can influence all moment tensor parameters: orientation, source type, and especially magnitude. Depth can be estimated from moment tensor inversions by fitting the spatial variation in surface waveform amplitudes. (The waveform shapes of body waves interacting with the free surface may also be used.) In many cases, however, waveform amplitudes may not be the best data for estimating the depth; in regional settings, for example, depths are typically estimated from  $P$  and  $S$  arrival times. We perform a grid search over depth for the 12 earthquakes in the Nevada Test Site, in order to compare the moment tensor depths with the depths from catalogs. We also examine the impact of choice of band pass. The complete set of depth test results are shown in Figures S9–S12. We find that the depth estimates from the moment tensor inversions are within a few kilometers of those from the catalogs. We choose to use the catalog-determined depths for the 12 earthquakes. Within our inversions we round the depths to the nearest kilometer (Table 2), which seems reasonable given that the uncertainty in depth is a few kilometers. Burial depths for the 17 nuclear tests are known to within a meter (Table 2); we fix all depths at 1 km. (See Ford et al., 2009, for a finer-scale treatment of event depth.)

## 5. Results

Our full results for all three catalogs (Table 1) are shown in full in Alvizuri (2017) as a set of plots of waveform fits and a set of plots of uncertainty analyses for all 116 events in this study and includes additional details for the 29 events from the Nevada Test Site.

Our three catalogs are displayed on two different source-type plots: the lune and the  $vw$  rectangle (Figure 3). Although these are source-type plots, encompassing two of six moment tensor parameters, we can depict the other four parameters by plotting the beach ball mechanism (three parameters for orientation) and coloring by magnitude. This catalog representation on the lune was introduced in Alvizuri and Tape (2016), but here we use the  $vw$  rectangle as well. Figure 3a depicts the previously published results from Ford et al. (2009), showing nuclear explosions, earthquakes, and collapses separated into three regions. Our results for the same 32 events are shown in Figure 3b. Our reanalysis of the 63 events from Uturuncu volcano are shown in Figure 3c. Our full moment tensor inversion results for 21 Alaska earthquakes are shown in Figure 3d.

### 5.1. Nevada Nuclear Tests

Following Ford et al. (2009), we use the 14 September 1991 HOYA nuclear test to illustrate the waveform fits and misfit analysis. We use 17 stations and filter surface waves at 7–33 s. A subset of waveform fits is shown in Figure 4, with the uncertainty summary in Figure 5. From our fine grid search over uniformly distributed moment tensors (section 3.2), we obtain a best-fitting moment tensor  $M_0$  with source type

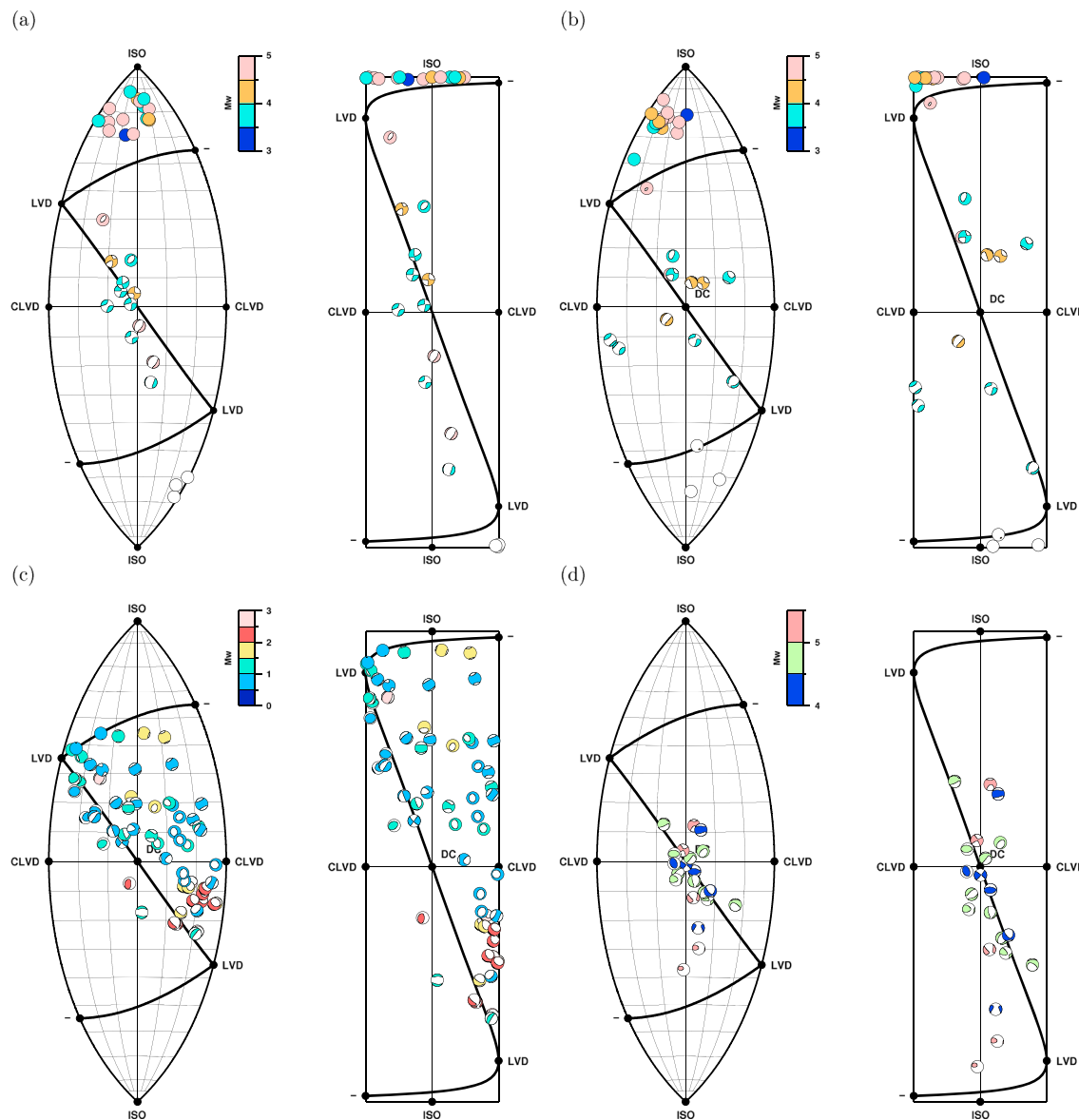


**Figure 3.** Full moment tensor catalogs, plotted on the lune (left) and on the vw rectangle (right; Figure 2). Beach balls are colored by magnitude. The plots convey all six parameters of the moment tensor: the source-type coordinates and magnitude characterize the eigenvalues of the moment tensor, while the beach ball conveys the orientation. Note that this representation does not convey the uncertainty for each event, as in Figure 5. (a) Ford et al. (2009) catalog of 32 earthquakes, explosions, and collapses from Nevada Test Site. (b) Same events as (a) but showing our solutions in this study. (c) Sixty-three events from Uturuncu volcano, Bolivia. (d) Twenty-one earthquakes from southern Alaska.

at  $(\gamma, \delta) = (-5^\circ, 66^\circ)$ . For easier visualization, we replace the random points by the points of a regular grid; this results in moving  $M_0$  to the point  $(\gamma, \delta) = (-5^\circ, 66^\circ)$ , enclosed by the green box in Figure 5. The best-fitting moment tensor is within the isotropic region defined by all-positive eigenvalues. (Note that the all-solid beach balls do not convey the variation in all-outward amplitudes that is present within this region.)

Our uncertainty summary figure in Figure 5 has two features not present in Alvizuri and Tape (2016). Figures 5e and 5f are relevant to the confidence curve, and Figure 5c shows the vw coordinate rectangle for source types (section 3.4). The function  $p(v, w)$  in Figure 5c is the inferred probability density, in the vw rectangle, for source types for the HOYA event. Conceptually, it is the correct concept, in the sense that the corresponding density for uniform moment tensors would be constant. Compared to the lune, the vw rectangle compresses the boundary regions of the lune, where moment tensors are more similar to each other. For the HOYA event, the maximum probability density is at the top of the vw rectangle in the positive isotropic region.

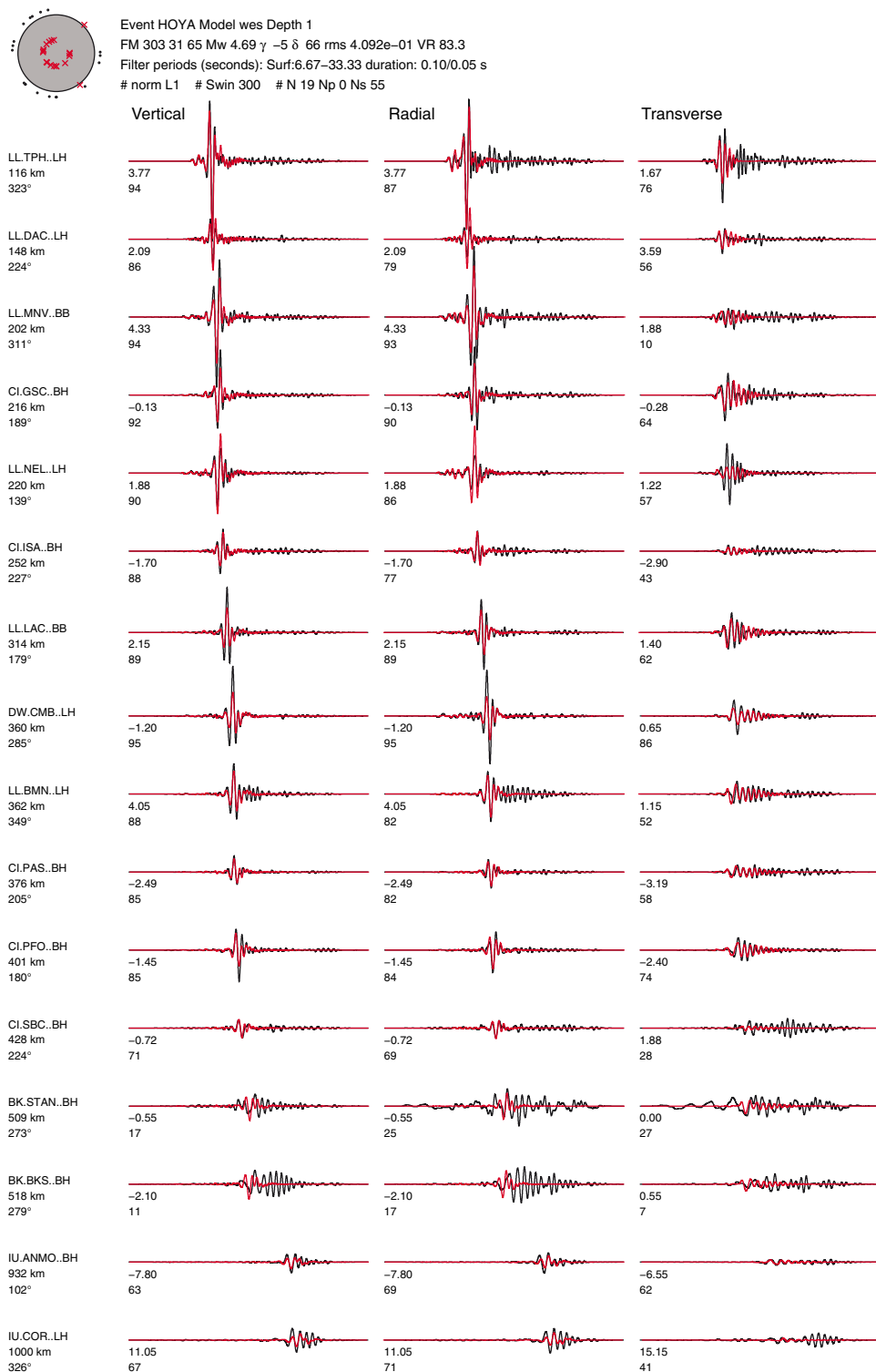


**Figure 4.** Moment tensor solution (top) and subset of waveform comparisons for the HOYA nuclear test on 14 September 1991; all waveforms used can be seen in Figure S16. The stations are ordered by increasing epicentral distance from the top row; the station distance and azimuth are labeled at left. The observed waveforms are plotted in black; the synthetic waveforms are plotted in red. Seismograms are filtered 7–33 s. The numbers below each station name are the station epicentral distance (top) and station azimuth (bottom). The two numbers below each pair of waveforms are (1) the cross-correlation time shift  $\Delta T = T_{\text{obs}} - T_{\text{syn}}$  required for matching the synthetics  $s(t)$  with the data  $u(t)$  (a positive time shift means that the synthetics arrive earlier than the data) and (2) the maximum cross-correlation percentage between  $u(t)$  and  $s(t - \Delta T)$ .

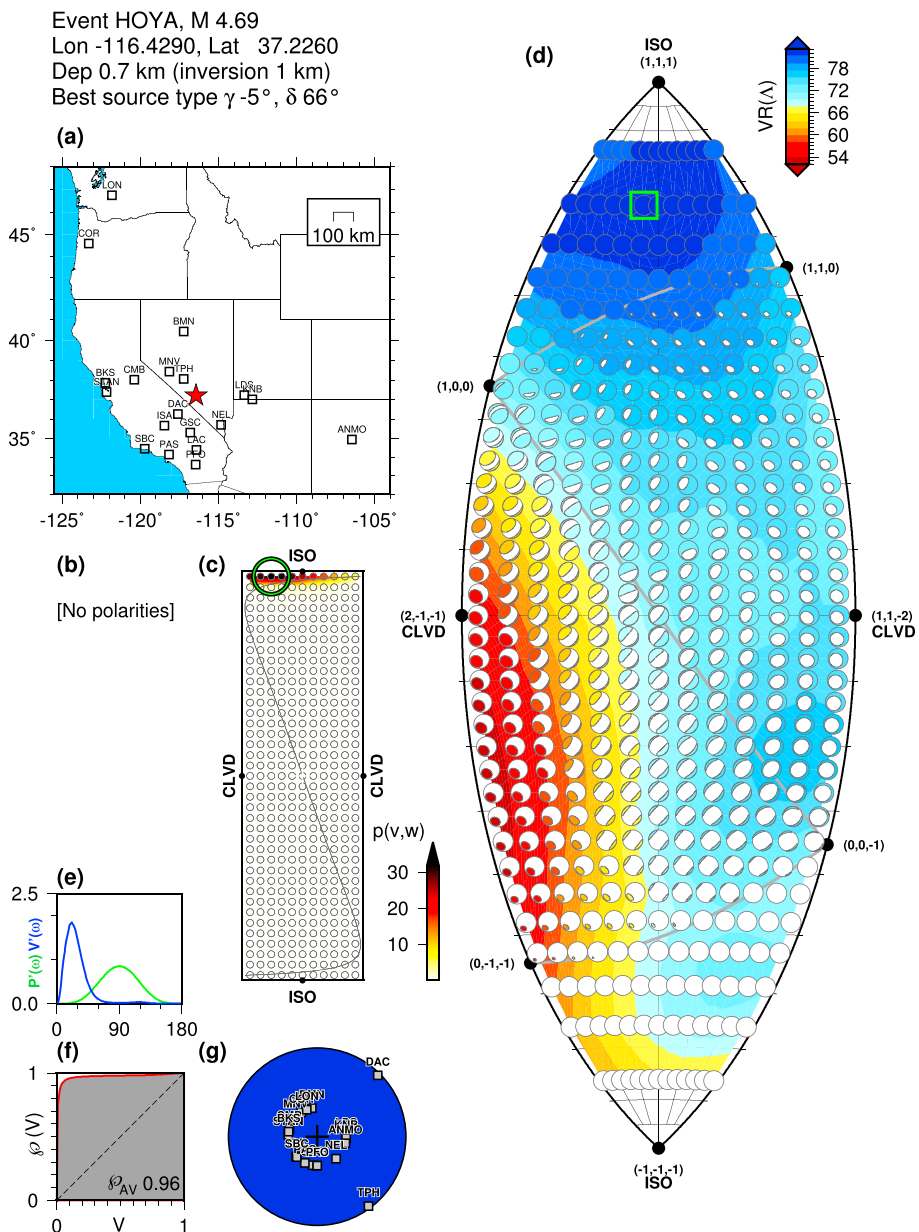


**Figure 5.** Full moment tensor uncertainty summary for the HOYA nuclear explosion. Waveforms for the best-fitting moment tensor are shown in Figure 4. (a) Map of source location (red star) and stations used in the inversion for this event. (b) Contour plot of the polarity misfit on the lune, if polarities had been used, as for the Uturuncu events (Alvizuri & Tape, 2016). (c) Source-type probability density  $p(v, w)$  in the  $vw$  rectangle (Tape & Tape, 2015). A green circle indicates the location of the point  $(v_x, w_x)$  where  $p$  is maximum; this point is apt to differ from the source type  $(v_0, w_0)$  of  $M_0$ . (d) Contour plot of the variance reduction  $VR(\Lambda)$ . At each point  $\Lambda$ , the variance reduction  $VR(\Lambda)$  is the maximum variance reduction  $VR(M)$  for moment tensors  $M$  that have source type  $\Lambda$ . Large values (blue) of  $VR$  represent better fit between observed and synthetic waveforms. Of the beach balls  $M(\Lambda)$ , our solution  $M_0$  (green box) is the one with the largest  $VR$ . The gray arcs on the lune are the great circle arcs  $\lambda_1 = 0$ ,  $\lambda_2 = 0$ , and  $\lambda_3 = 0$ ; they as well as other lune details are the same as in Figure 2, left. Selected eigenvalue triples (black dots) on the boundary of the lune are indicated, with the understanding that the triples need to be normalized. The positive isotropic source  $(1, 1, 1)$  is at the top, the negative isotropic source  $(-1, -1, -1)$  is at the bottom, and the double couple  $(1, 0, -1)$ , not shown, would be at the center of the lune. (e) The curves  $\hat{V}'(\omega)$  and  $\hat{P}'(\omega)$  that are used to construct the confidence curve  $\mathcal{P}(V)$  in (f), as explained in Silwal and Tape (2016) in the context of double couples. For full moment tensors, as here,  $\hat{V}'(\omega) \propto \sin^4 \omega$ . (f) The confidence curve  $\mathcal{P}(V)$  for  $M_0$ . The more the curve resembles the shape of a capital gamma ( $\Gamma$ ), the better. The shaded area is the average confidence  $\mathcal{P}_{av}$ . (g) The moment tensor  $M_0$ , plotted in a lower-hemisphere projection. The location of the piercing point for each station depends on the station azimuth, epicentral distance, and the assumed layered reference model.

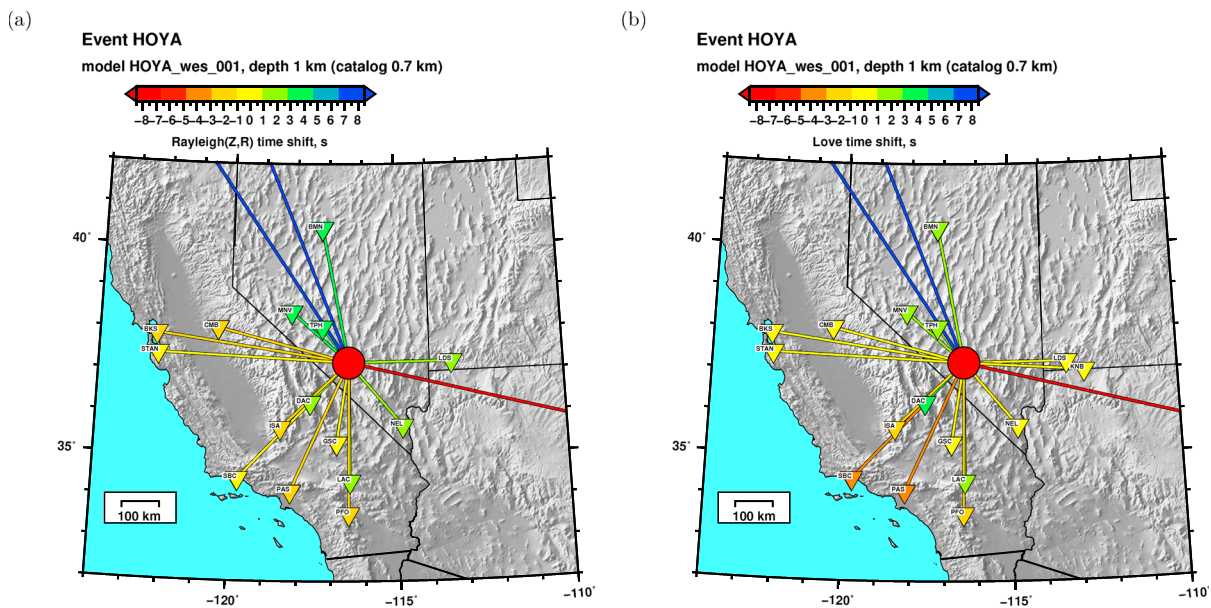


**Figure 6.** Surface wave time shifts used in the full moment tensor inversion for the HOYA nuclear test (Figure 4). Negative time shifts indicate that the reference model is too slow; positive time shifts indicate that the reference model is too fast. Plots for additional events are shown in Alvizuri (2017). (a) Rayleigh waves on vertical and radial components. (b) Love waves on transverse component.

We analyze spatial patterns of time shifts for Rayleigh waves and Love waves for each event. Time shift plots for HOYA are shown in Figure 6 and in Alvizuri (2017) for the other events. They reveal systematic variations with azimuth, which is what we would expect under the assumption of a 1-D Earth model. They also reveal variations with distance: for example, largest time shifts—positive 10 s to the northwest and negative 10 s to the east—occur for the longest paths ( $\sim 1,000$  km). These long-distance time shifts are identified from most of the events where the signal-to-noise ratio is sufficient at these distances (Alvizuri, 2017). We will discuss time shifts in section 6.3.

We calculate moment tensor solutions and uncertainty summaries for all of the 17 nuclear explosions treated by Ford et al. (2009). Figure 7 shows waveform fits for the best-fitting moment tensor for four nuclear tests: BEXAR, HORNITOS, BRISTOL, and DIVIDER. Uncertainty summary plots (e.g., Figure 5) for these events can be found in Alvizuri (2017); Figure 8 shows the variation of waveform misfit on the lune.

### 5.2. Uturuncu Volcanic Events

We reproduce the results from Alvizuri and Tape (2016) but using a modified misfit function. Previously, we excluded any moment tensor that had any disagreement between its predicted first-motion polarities and the observed first-motion polarities. The new, modified misfit function (equation (1)) balances the polarity misfit with the waveform misfit. This means that the misfit function is plotted on the entire lune, rather than on a subregion, as in Alvizuri and Tape (2016). The new, modified misfit function balances the polarity misfit with the waveform misfit. This means that the misfit function is plotted on the entire lune, rather than on a subregion, as in Alvizuri and Tape (2016). Figure 3c shows the full moment tensor catalog for 63 small ( $M_w < 3$ ) events at Uturuncu volcano. Most events in the catalog have a positive isotropic component ( $\delta > 0^\circ$ ), as before.

### 5.3. Alaska Earthquakes

We reexamine a set of 21 Alaska earthquakes, allowing for full moment tensors rather than just double-couple moment tensors, as in Silwal and Tape (2016). Figure 3d shows the full moment tensor solutions on the lune and on the  $vw$  rectangle. While some earthquakes exhibit a possibly spurious, negative isotropic component, most events are quite close to the double couple at the center of the lune. Full results are included in Alvizuri (2017).

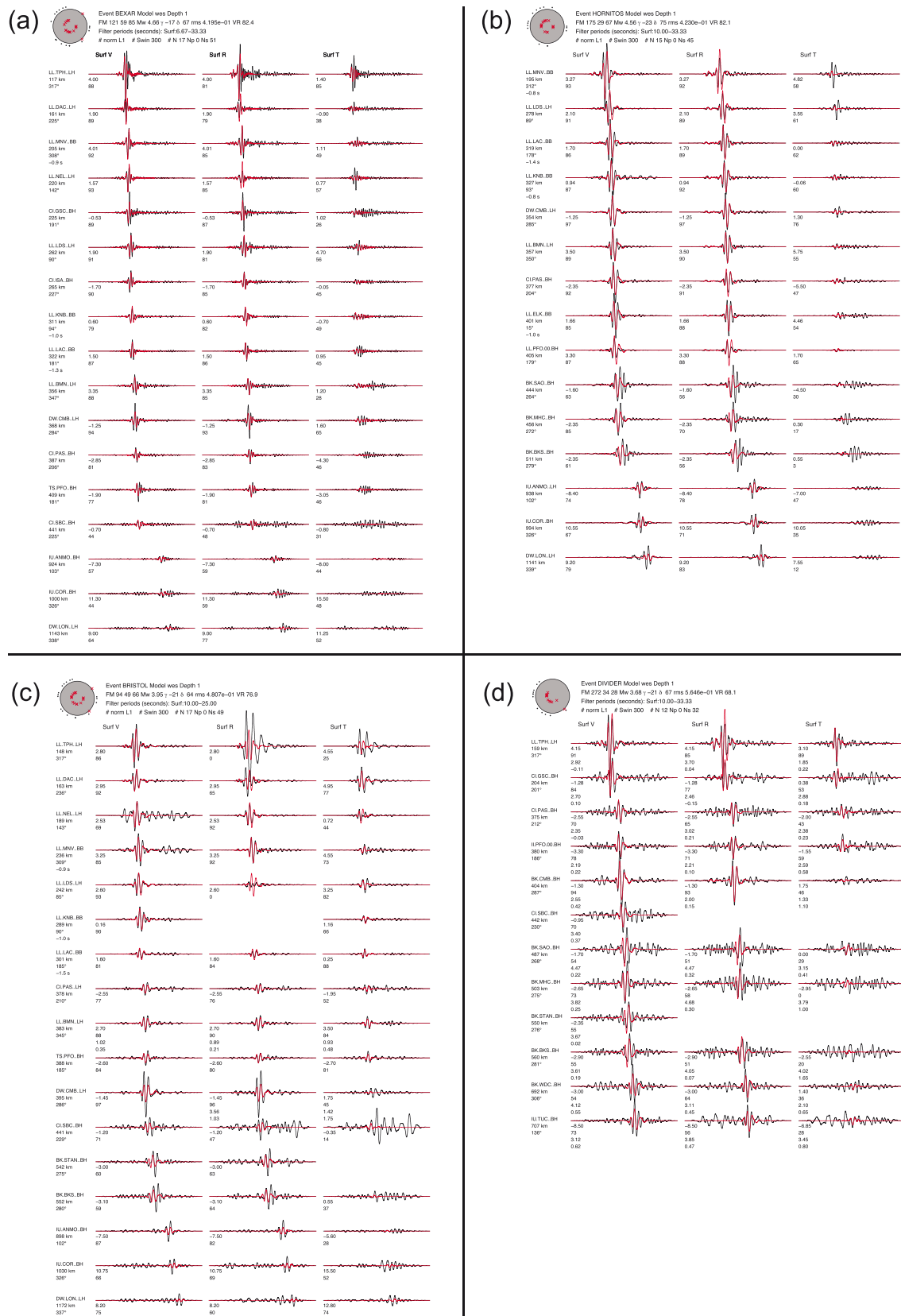


**Figure 7.** Waveform fits for four nuclear explosions: (a) BEXAR, (b) HORNITOS, (c) BRISTOL, and (d) DIVIDER. Additional events are shown in Alvizuri (2017). See Figure 8 for misfit plots on the lune.

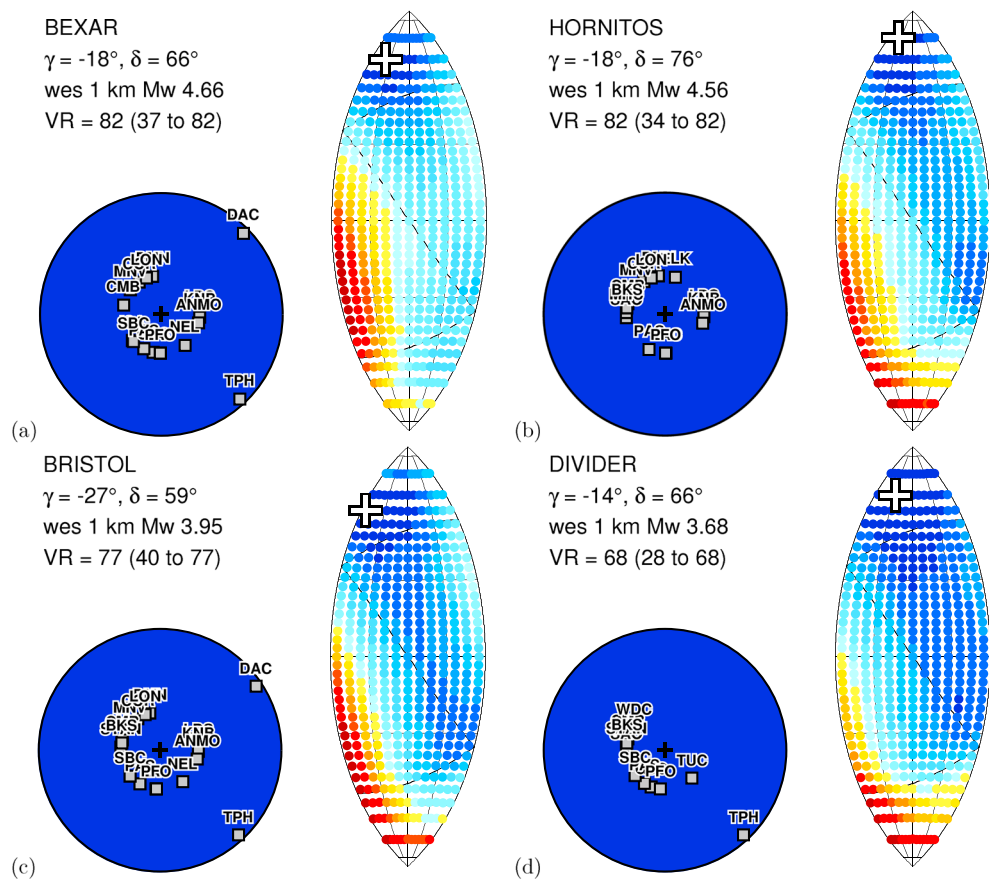


**Figure 8.** (a–d) Misfit plots on the lune for four examples of nuclear explosions whose best-fitting waveforms are shown in Figure 7. The color scale represents the variance reduction, from high (blue) at the best-fitting moment tensor to low (red); the min/max values are listed in the text label in each subplot and are adjusted to show the variation on the lune.

## 6. Discussion

### 6.1. Full Moment Tensor Inversions for Earthquakes

Earthquakes are useful for calibrating the results from nonearthquake events, such as nuclear explosions. Importantly, the full moment tensor inversions for earthquakes need to be performed with conditions that are as close as possible to the nonearthquake events, notably, same stations, same time period (meaning same station metadata), and similar epicentral region (similar paths). This was the motivation behind the event selection in Ford et al. (2009).

Earthquake mechanisms estimated as full moment tensors tend to cluster near the double-couple region of source-type space, as we might hope. However, the spread of best-fitting moment tensors can deviate significantly from the ideal double couple, as shown (Boyd et al., 2015, Figure 2a) for a set of 828 events in the Berkeley Seismological Laboratory catalog. Our full moment tensor analysis of 21 Alaska earthquakes exhibits a similar spread (Figure 3d). It is possible that this spread reflects true variations in source processes. However, we know from previous studies and from tests here that choices in the inversion play a significant role in obtaining a best-fitting moment tensor and event depth. The Berkeley moment tensor solutions typically use <8 stations and are based on low-pass-filtered surface waves (Dreger et al., 1998; Pasyanos et al., 1996). By comparison, our full moment tensor analysis of 21 Alaska earthquakes uses dozens of stations and also includes body waves, which can enhance the aperture of the source. In principle, improved data coverage and use of body waves should lead to better moment tensor solutions. If the true sources are exact double couples (which is probably unlikely), then we would expect the spread in source types to diminish when data coverage increases. Additional systematic studies are needed, such as the tests with double couples in Silwal and Tape (2016).

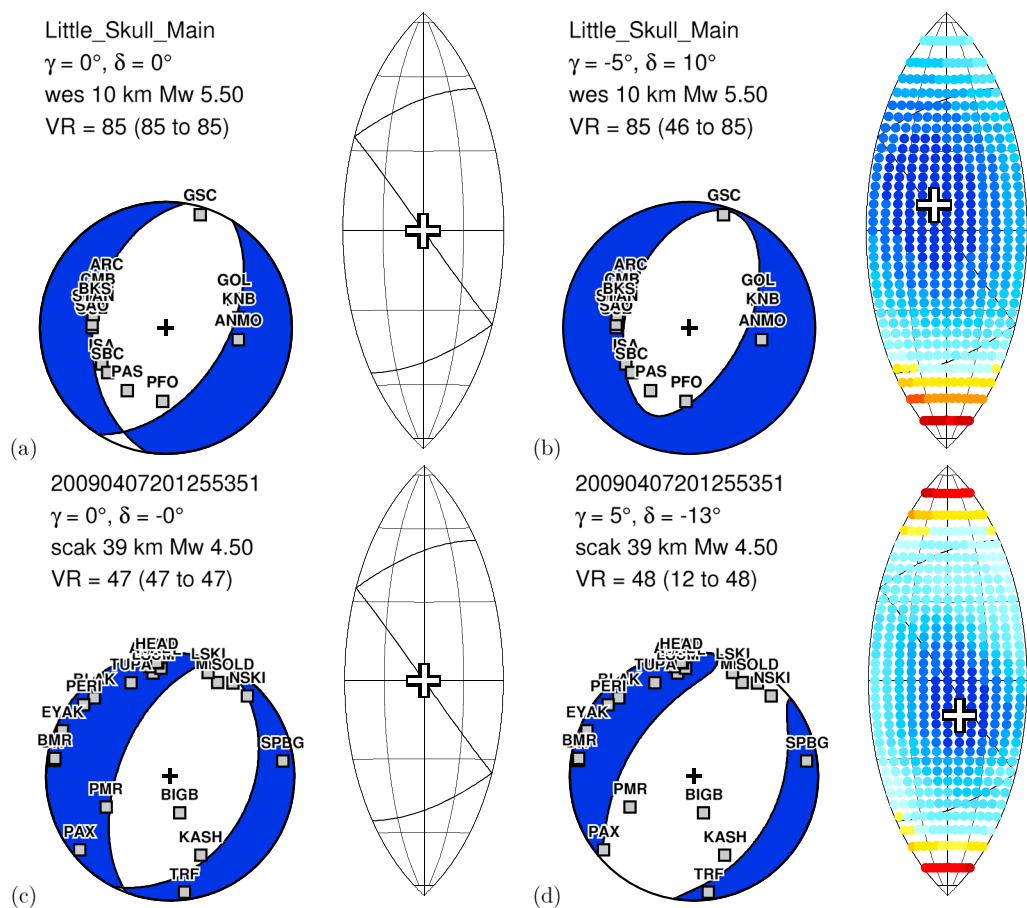


**Figure 9.** Comparison between double-couple moment tensors and full moment tensors for two earthquakes. (a) The best-fitting double couple for the Little Skull Mountain earthquake on 29 July 1992. (b) The best-fitting full moment tensor for the Little Skull Mountain earthquake. Waveform fits are shown in Figure S4. (c, d) Same as (a, b) but for a well-recorded Alaska earthquake on 7 April 2009.

In Figure 9 we further examine the double-couple constraint with two earthquakes. Because the full space of moment tensors is larger than the subspace of double-couple moment tensors, the best-fitting full moment tensor will give at least as good a fit to the data as does the double couple. The challenge is in deciding whether the improved fit warrants invoking some physical model (e.g., opening across a fault) over the traditional model of shear faulting. For the two earthquakes in Figure 9, the double couple is within the source-type region of good waveform fits, and we would probably attribute deviations from the double couple to variations in the data and modeling.

### 6.2. Inclusion of Body Waves

For moment tensor inversions in this study we have included waveform fits for body waves (Table 1). To examine the influence of body waves, we performed separate inversions with body waves only, surface waves only, and both combined. Results for the Little Skull Mountain earthquake and the HOYA nuclear test are shown in Figure 10. For the Little Skull Mountain earthquake the three mechanisms are different, though they all share a white central region and solid regions to the northwest and southeast.

For HOYA, we filtered body waves with 0.7–6.0 Hz. For the stations in the Lawrence Livermore National Laboratory database (Walter et al., 2006) we use the “HF” channel waveforms for the body waves and “BB” channel waveforms for the surface waves. (These waveforms are recorded by different sensors.) For the body waves, we align the synthetic *P* waves on the observed *P* onset times and then allow an additional cross-correlation time shift of only  $\pm 0.5$  s. The inversion with body waves only produces a moment tensor beach ball that is nearly all solid (Figure 10d). The effect of adding body waves to the surface waves-only inversion (Figure 10e) appears to be a concentrating of the best-fitting region on the lune (Figure 10f).

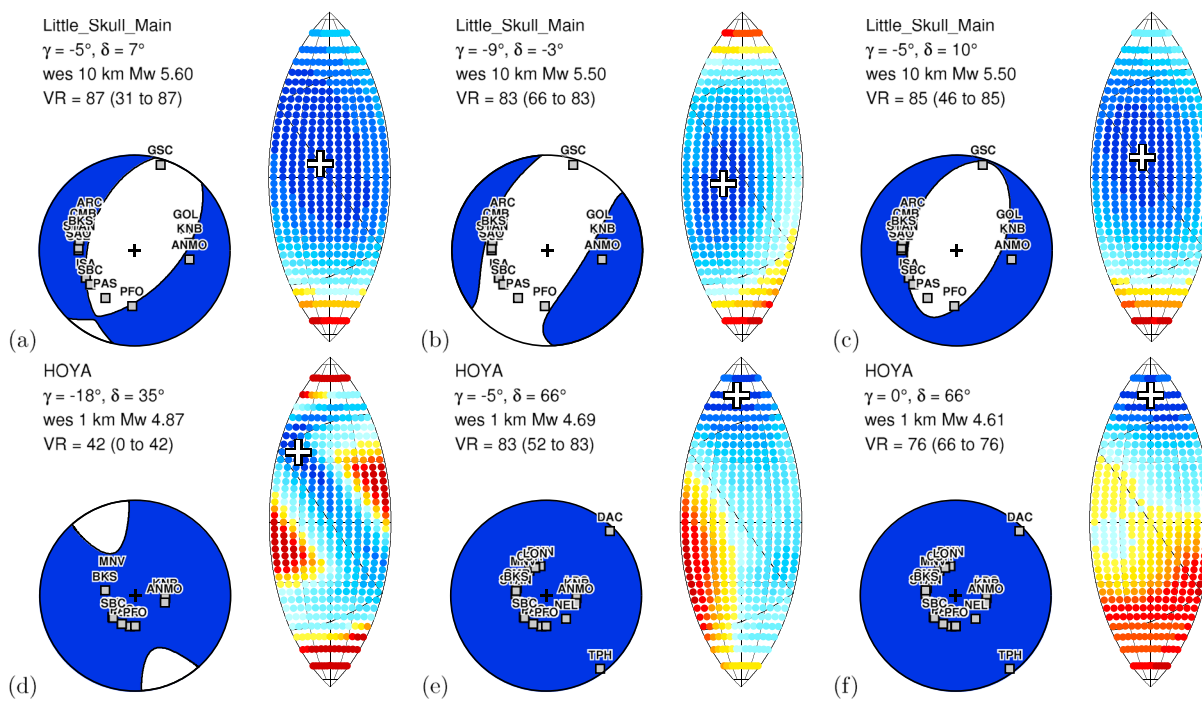


**Figure 10.** The influence of body waves and surface waves on moment tensor inversions for two example events. The lune shows  $VR(\Delta)$ , as in Figure 5c. The color scale is adjusted for each subplot in order to show the variation in  $VR(\Delta)$ . See section 6.2 for details. (a) Little Skull Mountain: body waves only; waveform fits in Figure S13. (b) Little Skull Mountain: surface waves only; waveform fits in Figure S4. (c) Little Skull Mountain: body waves and surface waves; waveform fits in Figure S4. (d) HOYA: body waves only; waveform fits in Figure S15. (e) HOYA: surface waves only; waveform fits in Figure 4 (and Figure S16), expanded version of uncertainty summary plot in Figure 5. (f) HOYA: body waves and surface waves; waveform fits in Figure S17. For HOYA, the best-fitting magnitudes were  $M_w$  4.87 (d),  $M_w$  4.69 (e), and  $M_w$  4.61 (f).

The two example events—the Little Skull Mountain earthquake and the HOYA nuclear test—produce very different  $P$  waveforms, due to their different source processes (earthquake versus explosion), their different magnitudes (Table 3:  $M_w$  5.5 versus  $M_w$  4.7), and their different source depths (Table 2: 10 km versus <1 km). Consequently, our preferred band passes for the body waves were very different: 5–100 s for Little Skull Mountain and 0.7–6 Hz for HOYA. From the HOYA results, we are encouraged that high-frequency regional  $P$  waveforms alone produce moment tensors that are similar to moment tensors produced from surface waves. Such  $P$  wave data, when combined with surface waves, should enhance the aperture of the source region while potentially providing detailed information about the source process, such as a source time function. Nevertheless, the amplitudes and shapes of high-frequency ( $f \geq 1$  Hz) waves are sensitive to structural effects at each site. These site effects may not be adequately characterized by our assumed 1-D model (or even by the best available 3-D models).

### 6.3. Time Shifts and Cycle Skipping

The application of time shifts to synthetic seismograms in moment tensor inversions is a widely used practice that can be both subtle and dangerous. As an extreme example, the moment tensor  $-M_0$  will exhibit the same relative variations in amplitudes as the best fitting moment tensor  $M_0$ ; therefore, with time shifts allowed, synthetic waveforms from  $-M_0$  may be similar to those of  $M_0$ . While the inclusion of first-motion polarity measurements can distinguish between these extreme cases, there are other cases that are difficult. With only 10 or so waveforms, as in the case of the NTS events (Table 2), a single misaligned waveform can influence the solution. One challenge is that the prospects of cycle skipping—misalignment of the synthetic wave with the observed wave—increase as we decrease the period content.

Whether using 1-D or 3-D velocity models to calculate synthetic seismograms, it is prudent to analyze time shifts between data and synthetics. We do this for each event for Rayleigh waves and Love waves, as shown in Figure 6. Abrupt changes in time shift with azimuth (for stations at similar distances) could be an indication of cycle skipping and also other effects: structural complexity along the path, errors in station metadata, errors in timing, or errors in the source representation, which can occur near nodal directions.

**Table 3**

Estimated Moment Tensors for Nuclear Explosions (17), Earthquakes (12), and Collapse Events (3)

Event	Stations used	Band-pass periods (s)			Strike $\kappa$	Dip $\theta$	Slip $\sigma$	$M_w$	Lune longitude $\gamma$	Lune latitude $\delta$	Poisson ratio $v$	Slip angle $\alpha$	Lune azimuth $\phi$	Crack fraction $\zeta$	$v$	$w$	$\mathcal{P}_{av}$
		7.7–50	6.7–33.3	10–50					longitude	latitude	ratio	azimuth	fraction				
KERNVILLE	13	6.7–50	21	40	77	4.58	–14	70	0.41	63	5	73	–0.23	1.18	0.96		
AMARILLO	12	10–33.3	263	41	50	4.12	–15	64	0.37	62	7	68	–0.24	1.17	0.79		
DISKO ELM	9	10–50	255	67	71	3.50	–25	51	0.21	36	19	71	–0.32	1.13	0.75		
HORNITOS	15	10–33.3	175	30	67	4.56	–23	75	0.40	42	6	81	–0.31	1.18	0.89		
BARNWELL	12	10–50	291	41	60	4.58	–5	62	0.45	81	3	62	–0.09	1.17	0.82		
METROPOLIS	12	6.7–33.3	183	33	63	4.18	–27	69	0.34	29	10	81	–0.33	1.18	0.84		
BULLION	9	6.7–33.3	160	61	85	4.99	–13	68	0.41	66	5	71	–0.21	1.17	0.85		
AUSTIN	11	6.7–25	131	60	88	3.49	1	69	0.51	92	–0	69	0.02	1.18	0.63		
HOUSTON	13	6.7–33.3	153	57	89	4.55	–17	67	0.38	58	7	72	–0.26	1.17	0.96		
COSO	14	6.7–50	246	22	43	3.46	–19	65	0.36	54	8	72	–0.28	1.17	0.59		
BEXAR	17	6.7–33.3	121	59	85	4.66	–17	67	0.38	59	7	71	–0.25	1.17	0.98		
HOYA	18	6.7–33.3	303	32	65	4.69	–5	66	0.46	82	2	66	–0.08	1.17	0.97		
LUBBOCK	14	6.7–33.3	113	69	87	4.05	–19	66	0.36	54	8	72	–0.28	1.17	0.81		
BRISTOL	17	10–25	94	49	66	3.95	–21	64	0.33	49	10	72	–0.30	1.17	0.75		
JUNCTION	15	6.7–33.3	153	57	89	4.63	–17	67	0.38	58	7	72	–0.26	1.17	0.96		
HUNTERS TROPHY	12	12.5–25	49	58	80	3.54	–20	65	0.35	50	9	73	–0.29	1.17	0.66		
DIVIDER	12	10–33.3	272	34	28	3.68	–21	67	0.35	48	9	74	–0.30	1.17	0.72		
Little Skull Main	15	10–50	33	50	–76	5.5	–5	11	0.12	81	26	15	–0.09	0.38	0.98		
Little Skull Aftershock	14	10–50	95	89	4	4.0	6	8	2.03	100	–36	14	0.10	0.28	0.97		
Timber Mountain	38	10–33.3	267	60	–20	3.7	3	–11	0.26	95	–165	13	0.05	–0.38	0.86		
Amargosa	30	10–25	26	71	–72	3.5	–4	17	0.27	82	14	19	–0.08	0.57	0.72		
Groom Pass	41	10–20	271	73	–36	3.8	–26	–11	–3.59	33	114	61	–0.33	–0.38	0.86		
Indian Springs	25	10–25	271	65	2	3.6	–23	–14	–14.03	42	122	53	–0.31	–0.47	0.85		
Calico Fan	50	10–25	74	54	–2	3.6	15	10	–91.09	117	–55	32	0.23	0.34	0.67		
Warm Springs	39	11.1–33.3	267	23	15	4.2	2	8	0.80	93	–13	9	0.03	0.29	0.63		
Frenchman Flat 1	11	10–33.3	60	52	–61	3.7	17	–25	0.04	123	–148	43	0.26	–0.78	0.64		
Frenchman Flat 2	55	10–33.3	229	49	–72	4.5	–16	41	0.22	60	18	51	–0.25	1.05	0.87		
Little Skull	82	6.7–33.3	45	66	–79	4.4	–6	–4	–21.44	79	123	14	–0.11	–0.15	0.83		
Ralston	88	10–33.3	264	83	–20	3.8	–5	11	0.17	82	22	14	–0.08	0.38	0.89		
ATRISCO Hole	3	6.7–50	305	19	–58	4.3	4	–66	0.47	96	–178	66	0.06	–1.17	0.85		
Trona Mine 1	9	10–50	52	80	–89	4.4	5	–48	0.42	99	–175	49	0.09	–1.11	0.65		
Trona Mine 2	35	12.5–33.3	105	30	–84	4.1	20	–61	0.32	130	–169	69	0.29	–1.17	0.63		

Note. See also Table 2. The source type for each moment tensor is listed in four different pairs: (1) lune longitude  $\gamma$  and lune latitude  $\delta$ , (2) Poisson ratio  $v$  and angle  $\alpha$  between slip vector and normal vector, (3) lune azimuth  $\phi$  and crack fraction  $\zeta$ , and (4)  $v$  and  $w$ . The last column lists the confidence parameter  $\mathcal{P}_{av}$ . See Alvizuri (2017) for complete results of all events.

Nuclear tests at the Nevada Test Site provide an interesting opportunity for examining time shifts because their hypocenters and origin times are known, and the tests are occurring in a similar region, leading to similar paths to distant stations. Therefore, we can aggregate the time shifts per station, as shown in Figure 11 for two example stations. These plots reveal several interesting points. First, as expected, we see much more consistent time shifts for the nuclear tests than we do for earthquakes. This can be attributed to uncertainties in the estimated source parameters (which can result in measured time shifts) and to the wider variation in earthquake depths and epicenters, leading to different Earth structures being sampled. Second, we see that time shifts from nuclear tests to stations vary systematically: positive time shifts to the north and east indicate that the 1-D model is too fast relative to the true Earth, while time shifts to the west and south tend to be slightly negative (e.g., Figure 6). Third, we find that Love and Rayleigh waves exhibit different time shifts,

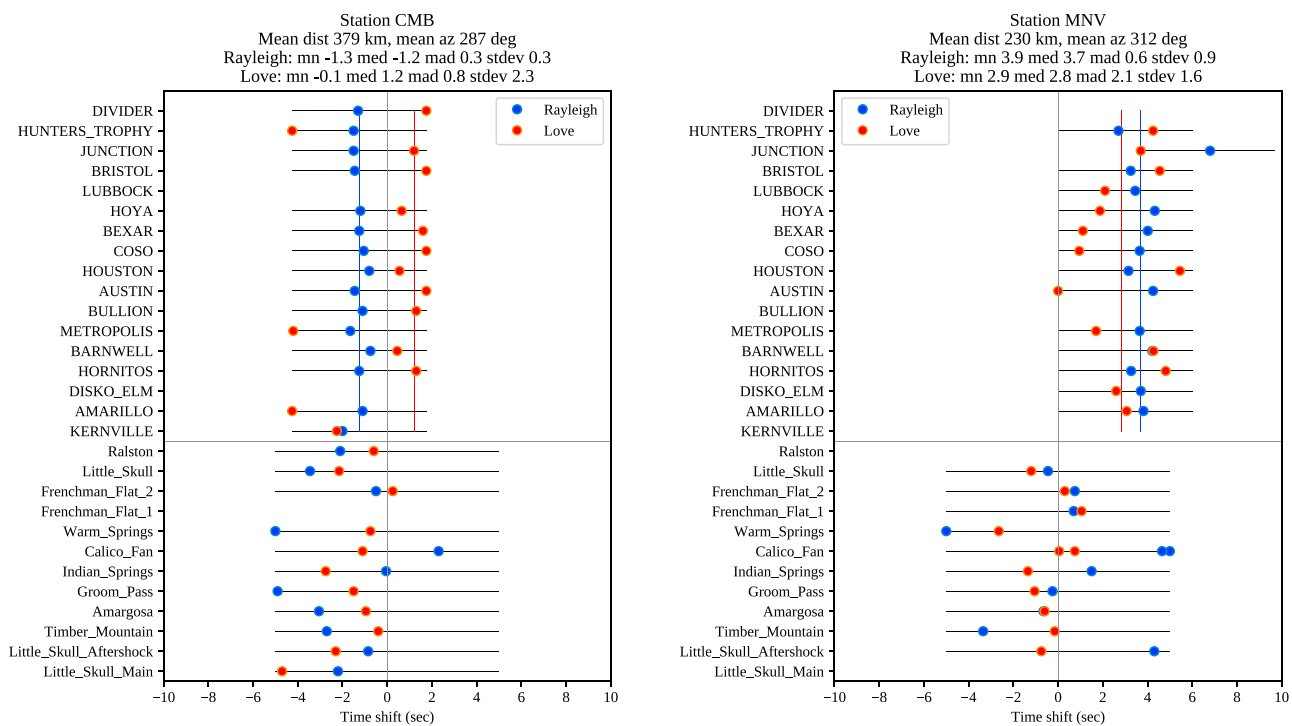


**Figure 11.** Surface wave time shifts for two example stations (CMB and MNV) for all 17 nuclear explosions and all 12 earthquakes in our study. (Missing events indicate that either the station did not record the event or the waveform was not used in the inversion.) Because all events are in or near the Nevada Test Site, the time shifts to the same station are expected to be similar. The Rayleigh waves time shifts for the nuclear events (upper 17 blue dots) provide the most consistent time shift estimate. The larger variance in time shifts for the earthquakes (lower 12 dots) is likely due to errors in source parameters (hypocenter and origin time) and also due to variability in event depths (Table 2). The horizontal black lines show the allowable range of the time shift. Plots for additional stations are shown in Alvizuri (2017).

and there is a suggestion, as in Figure 11 (and also DAC, LDS, and BWN in Alvizuri, 2017), that Love wave shifts are greater than Rayleigh wave time shifts. Such a discrepancy could arise from deficiencies in the 1-D velocity model, including consideration of (radial) anisotropy, which could produce a discrepancy between Love and Rayleigh waves. Finally, we note that the time shifts will depend on the selected band pass, since the validity of the 1-D model, in comparison to true Earth structure, will depend on the frequency of the waves. A frequency-dependent investigation (e.g., Tan et al., 2010) of time shifts could help assess the regions and depths where the 1-D model is a poor approximation for the real Earth structure. When including shorter periods, we expect to see stronger influences of 3-D Earth structure on the propagation path (“multipathing”) and on the development of the surface wave coda; an example is shown in Figures S6–S8.

The best approach to eliminating time shifts would be to use a 3-D velocity model that accurately predicts the arrival times of all waves used in the moment tensor inversion. For us, this would require accurate prediction of the seismic wavefield for periods  $\geq 1$  s. Such a regional model does not exist for any active tectonic setting, including the western United States. Cycle skipping of surface waves is particularly problematic, so one could have the more realistic goal of eliminating time shifts for periods  $\geq 5$  s. With dense data arrays and significant computational modeling, it is possible to fit the seismic wavefield at these periods (Lee et al., 2014; Tape et al., 2009). To integrate such a model into a moment tensor inversion would require replacing the computationally inexpensive, efficient calculation of 1-D synthetic seismograms with computationally expensive calculation of 3-D synthetic seismograms from wavefield simulations (Lee et al., 2011; Komatitsch et al., 2004; Zhao et al., 2006).

## 7. Summary

We present full moment tensor solutions, with uncertainties, for three sets of events: 29 events at the Nevada Test Site (plus 3 collapse events), 63 events at Uturuncu volcano, Bolivia, and 21 earthquakes in southern Alaska. We present a method to estimate the optimal moment tensor and magnitude from observed

waveforms. The method includes a grid search for magnitude, a grid search of the 5-D space of normalized moment tensors, and an estimate of uncertainty for moment tensors and their source types.

Our key findings are as follows:

1. The misfit function in moment tensor space exhibits local minima and other complexities. These reveal the importance of evaluating the misfit function over the full space of moment tensors, rather than using a linearized inversion, which may give a local minimum that is not a global minimum.
2. We provide a method for characterizing and visualizing the uncertainty for a full moment tensor. Our uncertainty summary, shown in Figure 5, has four components: (1) variation in waveform misfit for the best-fitting moment tensor at each lune point (Figure 5d), (2) probability density  $p(v, w)$  for moment tensor source type (Figure 5c), (3) confidence curve  $\mathcal{P}(V)$  (Figure 5f), (4) confidence parameter  $\mathcal{P}_{av}$ , which is the area under the confidence curve, with large values representing high concentration of probability near the best-fitting moment tensor  $M_0$ . For important events such as nuclear tests, a full display like Figure 5 may be useful. However, if a single parameter is desired, then the confidence parameter  $\mathcal{P}_{av}$  is a suitable option (Table 3).
3. The function  $\hat{P}(\omega)$  gives the probability that the true moment tensor is within angular distance  $\omega$  of the best moment tensor  $M_0$ . Although  $\hat{P}(\omega)$  is natural, it is misleading, and it needs to be interpreted in conjunction with the function  $\hat{V}(\omega)$ . The two functions are suitably combined in the confidence curve  $\mathcal{P}(V)$ . We are not clear how to expand our treatment of uncertainties beyond the 5-D parameter space—for example, with hypocenters, origin time, and source time functions (Stähler & Sigloch, 2014). It will require efficient sampling strategies for model parameter space and careful treatment in defining the homogeneous distribution.
4. We present a high-quality catalog of full moment tensors from the Nevada Test Site, building upon the efforts of Ford et al. (2009). The 17 nuclear tests were recorded between 1988 and 1992 during the early era of broadband seismology, and the limited station coverage at the time (Figure 1b) presents a challenge in estimating a moment tensor for each event. In comparison with Ford et al. (2009), we include more stations, we use a lower minimum period for all events (Table 3), and we include (regional) body waves in two inversions in order to demonstrate capabilities. The inclusion of body waves improves the coverage of the source hemisphere, since the body wave takeoff angles tend to be steep (and downward), whereas surface-wave paths are near horizontal. We present full results of the inversions in Alvizuri (2017), allowing for easier reproducibility and improvements for future research efforts.

Further efforts to include additional body waves from broadband stations or first-motion polarity measurements from short-period stations (Harmsen, 1994) could result in moment tensor solutions with higher confidence than those presented here.

Additional work is needed to improve the theory and application of moment tensor confidence curves. Many choices are made regarding the misfit function; they include time windowing, weighting, choice of norm, and time shifting of synthetic seismograms. For example, a more complete representation of data covariance terms (e.g., Mustać & Tkalčić, 2016; Stähler & Sigloch, 2016) could eliminate the need for a scale factor. The use of 3-D synthetic seismograms could lessen the need for time shifts, if the 3-D velocity model is accurate. Some questions can be adequately addressed without real data, within synthetic inversions (Staněk et al., 2014; Stierle et al., 2014; Walter et al., 2010; Wéber, 2006).

## Acknowledgments

Seismic waveform data and station metadata used in this study are available from the IRIS Data Management Center, either from within its own archives or from the assembled data set of Walter et al. (2006). A complete set of results from our moment tensor catalogs is available at Alvizuri (2017). We thank Walt Tape for feedback on the manuscript. We thank Matt Gardine and Michael West for help in reading the database of Walter et al. (2006). The manuscript benefitted from reviews by Sean Ford and Doug Dreger. This project was supported by the Air Force Research Laboratory (contracts FA9453-15-C-0063 and FA9453-17-C-0025) and the National Science Foundation (grant EAR-1215959). The work of C.A. was partially supported by the Swiss National Science Foundation (grant PP00P2 157627: OROG3NY).

## References

- Aki, K., & Richards, P. G. (2002). *Quantitative seismology* (2nd ed.). San Francisco, CA: University Science Books. 2009 corrected printing.
- Alvizuri, C. (2017). Moment tensor catalog results for nuclear explosions, volcanic events, and earthquakes, ScholarWorks@UA at <http://hdl.handle.net/11122/8007> (last accessed 2018-05-07): descriptor file, text files of catalogs, and composite figures of waveform fits, uncertainty results, and time shifts.
- Alvizuri, C., & Tape, C. (2016). Full moment tensors for small events ( $M_w < 3$ ) at Uturuncu volcano, Bolivia. *Geophysical Journal International*, 206, 1761–1783. <https://doi.org/10.1093/gji/ggw247>
- Bennett, T. J., Oancea, V., Barker, B. W., Kung, Y.-L., Bahavar, M., Kohl, B. C., et al. (2010). The Nuclear Explosion Database (NEDB): A new database and web site for accessing nuclear explosion source information and waveforms. *Seismological Research Letters*, 81(1), 12–25. <https://doi.org/10.1785/gssrl.81.1.12>
- Beyreuther, M., Barsch, R., Krischer, L., Megies, T., Behr, Y., & Wassermann, J. (2010). ObsPy: A Python toolbox for seismology. *Seismological Research Letters*, 81(3), 530–533. <https://doi.org/10.1785/gssrl.81.3.530>
- Boyd, O. S., Dreger, D. S., Lai, V. H., & Gritto, R. (2015). A systematic analysis of seismic moment tensor at The Geysers geothermal field, California. *Bulletin of the Seismological Society of America*, 105(6), 2969–2986. <https://doi.org/10.1785/0120140285>
- Chiang, A., Dreger, D. S., Ford, S. R., & Walter, W. R. (2014). Source characterization of underground explosions from combined regional moment tensor and first-motion analysis. *Bulletin of the Seismological Society of America*, 104(4), 1587–1600. <https://doi.org/10.1785/0120130228>

- Dreger, D., Uhrhammer, R., Pasanos, M., Franck, J., & Romanowicz, B. (1998). Regional and far-regional earthquake locations and source parameters using sparse broadband networks: A test on the Ridgecrest sequence. *Bulletin of the Seismological Society of America*, 88(6), 1353–1362.
- Dziewonski, A., Chou, T.-A., & Woodhouse, J. H. (1981). Determination of earthquake source parameters from waveform data for studies of global and regional seismicity. *Journal of Geophysical Research*, 86(B4), 2825–2852. <https://doi.org/10.1029/JB086iB04p02825>
- Ekström, G., Nettles, M., & Dziewoński, A. M. (2012). The global GCMT project 2004–2010: Centroid-moment tensors for 13,017 earthquakes. *Physics of the Earth and Planetary Interiors*, 200–201, 1–9. <https://doi.org/10.1016/j.pepi.2012.04.002>
- Ford, S. R., Dreger, D. S., & Walter, W. R. (2009). Identifying isotropic events using a regional moment tensor inversion. *Journal of Geophysical Research*, 114, B01306. <https://doi.org/10.1029/2008JB005743>
- Ford, S. R., Dreger, D. S., & Walter, W. R. (2010). Network sensitivity solutions for regional moment-tensor inversions. *Bulletin of the Seismological Society of America*, 100(5A), 1962–1970. <https://doi.org/10.1785/0120090140>
- Ford, S. R., Walter, W. R., & Dreger, D. S. (2012). Event discrimination using regional moment tensors with teleseismic-P constraints. *Bulletin of the Seismological Society of America*, 102(2), 867–872. <https://doi.org/10.1785/0120110227>
- Gomberg, J., & Bodin, P. (1994). Triggering of the  $M_s = 5.4$  Little Skull Mountain, Nevada, earthquake with dynamic strains. *Bulletin of the Seismological Society of America*, 84(3), 844–853.
- Harmsen, S. C. (1994). The Little Skull Mountain, Nevada, earthquake of 29 June 1992: Aftershock focal mechanisms and tectonic stress field implications. *Bulletin of the Seismological Society of America*, 84(5), 1484–1505.
- Haskell, N. (1964). Total energy and energy spectral density of elastic wave radiation from propagating faults. *Bulletin of the Seismological Society of America*, 54, 1811–1842.
- Keyson, L., & West, M. E. (2013). Earthquake sources near Uturuncu Volcano. In *Abstract V13B-2603 presented at 2013 Fall Meeting*, AGU, San Francisco, California.
- Komatitsch, D., Liu, Q., Tromp, J., Süss, P., Stidham, C., & Shaw, J. H. (2004). Simulations of ground motion in the Los Angeles basin based upon the spectral-element method. *Bulletin of the Seismological Society of America*, 94(1), 187–206. <https://doi.org/10.1785/0120030077>
- Krischer, L., Mengies, T., Barsch, R., Beyreuther, M., Lecocq, T., Caudron, C., & Wassermann, J. (2015). ObsPy: A bridge for seismology into the scientific Python ecosystem. *Computational Science & Discovery*, 8(1), 014003. <https://doi.org/10.1088/1749-4699/8/1/014003>
- Lee, E.-J., Chen, P., Jordan, T. H., Maechling, P. B., Denolle, M. A. M., & Beroza, G. C. (2014). Full-3-D tomography for crustal structure in Southern California based on the scattering-integral and the adjoint-wavefield methods. *Journal of Geophysical Research: Solid Earth*, 119, 6421–6451. <https://doi.org/10.1002/2014JB011346>
- Lee, E.-J., Chen, P., Jordan, T. H., & Wang, L. (2011). Rapid full-wave centroid moment tensor (CMT) inversion in a three-dimensional earth structure model for earthquakes in Southern California. *Geophysical Journal International*, 186, 311–330. <https://doi.org/10.1111/j.1365-246X.2011.05031.x>
- Lohman, R. B., Simons, M., & Savage, B. (2002). Location and mechanism of the Little Skull Mountain earthquake as constrained by satellite radar interferometry and seismic waveform modeling. *Journal of Geophysical Research*, 107(B6), 2118. <https://doi.org/10.1029/2001JB000627>
- Mustać, M., & Tkalčić, H. (2016). Point source moment tensor inversion through a Bayesian hierarchical model. *Geophysical Journal International*, 204, 311–323. <https://doi.org/10.1093/gji/ggv458>
- Nayak, A., & Dreger, D. S. (2014). Moment tensor inversion of seismic events associated with the sinkhole at Napoleonville salt dome, Louisiana. *Bulletin of the Seismological Society of America*, 104(4), 1763–1776. <https://doi.org/10.1785/0120130260>
- Pasanos, M. E., Dreger, D. S., & Romanowicz, B. (1996). Toward real-time estimation of regional moment tensors. *Bulletin of the Seismological Society of America*, 86(5), 1255–1269.
- Pesicek, J. D., Ciešlik, K., Lambert, M.-A., Carrillo, P., & Birkelo, B. (2016). Dense surface seismic data confirm non-double-couple source mechanisms induced by hydraulic fracturing. *Geophysics*, 81(6), KS207–KS217. <https://doi.org/10.1190/GEO2016-0192.1>
- Pesicek, J. D., Sileny, J., Prejean, S. G., & Thurber, C. H. (2012). Determination and uncertainty of moment tensors for microearthquakes at Okmok Volcano, Alaska. *Geophysical Journal International*, 190, 1689–1709. <https://doi.org/10.1111/j.1365-246X.2012.05574.x>
- Ross, Z. E., Ben-Zion, Y., & Zhu, L. (2015). Isotropic source terms of San Jacinto fault zone earthquakes based on waveform inversions with a generalized CAP method. *Geophysical Journal International*, 200, 1267–1278. <https://doi.org/10.1093/gji/ggu460>
- Šílený, J., & Milev, A. (2006). Seismic moment tensor resolution on a local scale: Simulated rockburst and mine-induced seismic events in the Kopanang gold mine, South Africa. *Pure and Applied Geophysics*, 163, 1495–1513. <https://doi.org/10.1007/s00024-006-0089-z>
- Silwal, V., & Tape, C. (2016). Seismic moment tensors and estimated uncertainties in southern Alaska. *Journal of Geophysical Research: Solid Earth*, 121, 2772–2797. <https://doi.org/10.1002/2015JB012588>
- Song, X. J., Helmberger, D. V., & Zhao, L. (1996). Broad-band modelling of regional seismograms: The Basin and Range crustal structure. *Geophysical Journal International*, 125, 15–29.
- Springer, D. L., Pawloski, G. A., Ricca, J. L., Rohrer, R. F., & Smith, D. K. (2002). Seismic source summary for all U.S. below-surface nuclear explosions. *Bulletin of the Seismological Society of America*, 92(5), 1806–1840. <https://doi.org/10.1785/0120010194>
- Stähler, S. C., & Sigloch, K. (2014). Fully probabilistic seismic source inversion—Part 1: Efficient parameterisation. *Solid Earth*, 5, 1055–1069. <https://doi.org/10.5194/se-5-1055-2014>
- Stähler, S. C., & Sigloch, K. (2016). Fully probabilistic seismic source inversion—Part 2: Modelling errors and station covariances. *Solid Earth*, 7, 1521–1536. <https://doi.org/10.5194/se-7-1521-2016>
- Stanek, F., Eisner, L., & Moser, T. J. (2014). Stability of source mechanisms inverted from P-wave amplitude microseismic monitoring data acquired at the surface. *Geophysical Prospecting*, 62, 475–490. <https://doi.org/10.1111/1365-2478.12107>
- Stierle, E., Vavryčuk, V., Šílený, J., & Bohnhoff, M. (2014). Resolution of non-double-couple components in the seismic moment tensor using regional networks—I: A synthetic case study. *Geophysical Journal International*, 196, 1869–1877. <https://doi.org/10.1093/gji/ggt502>
- Tan, Y., Song, A., Wei, S., & Helmberger, D. (2010). Surface wave path corrections and source inversions in southern California. *Bulletin of the Seismological Society of America*, 100(6), 2891–2904. <https://doi.org/10.1785/0120090063>
- Tape, C., Liu, Q., Maggi, A., & Tromp, J. (2009). Adjoint tomography of the southern California crust. *Science*, 325, 988–992. <https://doi.org/10.1126/science.1175298>
- Tape, W., & Tape, C. (2012). A geometric setting for moment tensors. *Geophysical Journal International*, 190, 476–498. <https://doi.org/10.1111/j.1365-246X.2012.05491.x>
- Tape, W., & Tape, C. (2013). The classical model for moment tensors. *Geophysical Journal International*, 195, 1701–1720. <https://doi.org/10.1093/gji/ggt302>
- Tape, W., & Tape, C. (2015). A uniform parameterization of moment tensors. *Geophysical Journal International*, 202, 2074–2081. <https://doi.org/10.1093/gji/ggv262>

- Tape, W., & Tape, C. (2016). A confidence parameter for seismic moment tensors. *Geophysical Journal International*, 205, 938–953. <https://doi.org/10.1093/gji/ggw057>
- Vavryčuk, V. (2011). Tensile earthquakes: Theory, modeling, and inversion. *Journal of Geophysical Research*, 116, B12320. <https://doi.org/10.1029/2011JB008770>
- Walter, F., Dreger, D. S., Clinton, J. F., Deichmann, N., & Funk, M. (2010). Evidence for near-horizontal tensile faulting at the base of Gornergletscher, a Swiss Alpine Glacier. *Bulletin of the Seismological Society of America*, 100(2), 458–472. <https://doi.org/10.1785/0120090083>
- Walter, W. R., Smith, K. D., O'Boyle, J. L., Hauk, T. F., Ryall, F., Ruppert, S. D., et al. (2006). An assembled western United States dataset for regional seismic analysis, ISSO 9660 CD, LLNL release UCRL-MI-222502, Retrieved from <https://ds.iris.edu/mda/18-001>
- Wéber, Z. (2006). Probabilistic local waveform inversion for moment tensor and hypocentral location. *Geophysical Journal International*, 165, 607–621.
- Zhao, L., Chen, P., & Jordan, T. H. (2006). Strain Green's tensors, reciprocity, and their applications to seismic source and structure studies. *Bulletin of the Seismological Society of America*, 96(5), 1753–1763. <https://doi.org/10.1785/0120050253>
- Zhao, L.-S., & Helmberger, D. V. (1994). Source estimation from broadband regional seismograms. *Bulletin of the Seismological Society of America*, 84(1), 91–104.
- Zhu, L., & Ben-Zion, Y. (2013). Parameterization of general seismic potency and moment tensors for source inversion of seismic waveform data. *Geophysical Journal International*, 194, 839–843. <https://doi.org/10.1093/gji/ggt137>
- Zhu, L., & Helmberger, D. (1996). Advancement in source estimation techniques using broadband regional seismograms. *Bulletin of the Seismological Society of America*, 86(5), 1634–1641.
- Zhu, L., & Rivera, L. A. (2002). A note on the dynamic and static displacements from a point source in multilayered media. *Geophysical Journal International*, 148, 619–627. <https://doi.org/10.1046/j.1365-246X.2002.01610.x>